

# Data Driven Modeling of Interfacial Traction Separation Relations using a Thermodynamically Consistent Neural Network

Congjie Wei<sup>1</sup>, Jiaxin Zhang<sup>2</sup>, Kenneth M. Liechti<sup>3</sup>, Chenglin Wu<sup>1\*</sup>,

<sup>1</sup>Department of Civil, Architectural, and Environmental Engineering  
Missouri University of Science and Technology, Rolla, MO, USA

<sup>2</sup>Computer Science and Mathematics Division

Oak Ridge National Laboratory, Oak Ridge, TN 37830

<sup>3</sup>Center for the Mechanics of Solids, Structures and Materials

Department of Aerospace Engineering and Engineering Mechanics

The University of Texas at Austin, Austin, TX, USA

\* Corresponding author E-mail: [zhangj@ornl.gov](mailto:zhangj@ornl.gov), [wuch@mst.edu](mailto:wuch@mst.edu)

## Abstract

For multilayer structures, interfacial failure is one of the most important elements related to device reliability. For cohesive zone modelling, traction-separation relations represent the adhesive interactions across interfaces. However, existing theoretical models do not currently capture traction-separation relations that have been extracted using direct methods, particularly under mixed-mode conditions. Given the complexity of the problem, models derived from the neural network approach are attractive. Although they can be trained to fit data along the loading paths taken in a particular set of mixed-mode fracture experiments, they may fail to obey physical laws for paths not covered by the training data sets. In this paper, a thermodynamically consistent neural network (TCNN) approach is established to model the constitutive behavior of interfaces when faced with sparse training data sets. Accordingly, three conditions are examined and implemented here: (i) thermodynamic consistency, (ii) maximum energy dissipation path control and (iii) J-integral conservation. These conditions are treated as constraints and are implemented as such in the loss function. The feasibility of this approach is demonstrated by comparing the modeling results with a range of physical constraints. Moreover, a Bayesian optimization algorithm is then adopted to optimize the weight factors associated with each of the constraints in order to overcome convergence issues that can arise when multiple constraints are present. The resultant numerical implementation of the ideas presented here produced well-behaved, mixed-mode traction separation surfaces that maintained the fidelity of the experimental data that was provided as input. The proposed approach heralds a new autonomous, point-to-point constitutive modeling concept for interface mechanics.

**Keywords:** Interface mechanics; Cohesive zone modelling; Traction-separation relations; Physics constrained neural networks; Machine learning; Bayesian optimization.

## Nomenclature

<b>Abbreviation</b>	<b>Meaning</b>
MSE	Mean squared error
TC	Thermodynamically consistent
TC1	Positive energy dissipation constraint
TC2	Maximum energy dissipation constraint
TC3	J-integral conservation constraint
TCNN	Thermodynamically consistent neural network

<b>Symbol</b>	<b>Description</b>
$\delta_n, \delta_t$	Normal and tangential separation
$\sigma_n, \sigma_t$	Normal and tangential traction
$ \delta ,  \sigma $	Separation, traction norms
$\phi$	Phase angle
$J_n, J_t, J$	Normal, tangential, and total J-integral
$d_n, d_t$	Normal and tangential damage parameters
$\Gamma_n, \Gamma_t$	Normal and tangential toughness
$\theta$	Loading angle on the damage surface
$X, Y$	Input and output data sets

$MSE_0$	Loss function term corresponding to mean squared error
$MSE_1, MSE_2, MSE_3$	Loss function terms incorporating the TC1, TC2 and TC3 constraints
$\lambda_0$	Weight factor assigned to the mean squared error
$\lambda_1, \lambda_2, \lambda_3$	Weight factors assigned to the TC1, TC2 and TC3 constraints
$\epsilon_{phi}$	Angle difference
$Vio_1, Vio_2, Vio_3$	Violations of the TC1, TC2 and TC3 conditions
$\overline{Vio_1}, \overline{Vio_2}, \overline{Vio_3}$	Normalized violations of the TC1, TC2 and TC3 conditions

## 1. Introduction

First proposed by Dugdale and Barrenblatt (Dugdale 1960, Barrenblatt 1962), cohesive zone models have been widely adopted to describe nonlinear fracture processes, especially for interfacial fracture where fracture paths are often pre-determined (Ungsuwarungsri and Knauss 1987, Needleman 1990, Elices, Guinea et al. 2002, Yang and Cox 2005, Turon, Camanho et al. 2010). Typically, cohesive zone models take pre-determined traction-separation relations as input either through cohesive elements or cohesive contact formulations in finite element codes to portray interfacial crack growth. Based on how traction-separation relations are implemented, cohesive zone models can be divided into those that are based on potentials or displacements (Park, Choi et al. 2016). The displacement approach typically uses specific forms of traction-separation relations including bilinear softening (Wittmann, Rokugo et al. 1988), cubic-polynomial (Dong, Chen et al. 2019), linear-softening (Camanho, Davila et al. 2003) and exponential (Park and Paulino 2013, McGarry, Máirtín et al. 2014). However, the physics behind the traction-separation relations that are used in this approach is not typically considered.

To ensure that the input traction-separation relations conform to the principles of thermodynamics, the potential-based models are based on the concept of cohesive energy potentials where the normal and tangential separations are adopted as independent variables. Cohesive tractions are defined as gradients of the cohesive energy potentials over separations for the softening stage. Needleman (1987) pioneered the potential-based approach by introducing cubic-linear and exponential interfacial debonding potentials. Freed and Bank-Sills (2008) extended the application to bi-material systems. Other types of potentials were also explored, including atomistic potentials relating metallic binding energies to lattice parameters (Rose, Ferrante et al. 1981), exponential-periodic potential adopting large tangential displacement jumps (Needleman 1990) and generalized exponential-periodic potential considering the relation between cleavage decohesion and dislocation nucleation (Beltz and Rice 1991). These potential-based models are thermodynamically consistent and have a certain degree of flexibility to accommodate some of the behavior that has been observed in experiments. However, when dissipative interfacial failure mechanisms are involved, the potential-based approach often faces challenges in fitting the experimental data. Consequently, there is a need to develop a data-driven approach to model interfacial traction-separation relations that can capture the richness of the experimental data while remaining thermodynamically consistent. To this end, we seek a way to

combine a data-driven approach, specifically deep learning, with thermodynamically consistent constraints in order to deliver a universal approach to model interfacial traction-separation relations that are extracted directly from experiments.

The deep learning approach has already been incorporated in computational fluid mechanics, where it is used to solve the governing partial differential equations of the fluid field (Kutz 2017, Wang, Xiao et al. 2018, Brunton, Noack et al. 2020) and constitutive modeling in plasticity (Eggersmann, Kirchdoerfer et al. 2019, Huang, Fuhs et al. 2020, Weber, Pinz et al. 2020). The deep neural network generates potential solutions in terms of the displacement or velocity field that do satisfy the field equations. Building on these developments, the authors employ a deep neural network to learn from the traction-separation relations that are extracted from experiments along discrete mixed-mode loading paths, in order to generate traction surfaces in the mixed-mode space defined by the amplitude and phase of the interfacial separation vector. Thermodynamically consistent constraints that enforce positive energy dissipation, local maxima in energy dissipation, as well as the conservation of the J-integral, are embedded in this deep neural network framework to form a thermodynamically consistent neural network (TCNN) for generating surfaces for traction-separation relations. The hyperparameter system, which is used for tuning the learning process, plays an essential role in the performance of neural networks. When inappropriate hyperparameter sets are adopted, convergence can be harder to achieve and important features of traction-separation relations may be missed and lack robustness. Efforts have been made to develop algorithms for hyperparameter optimization, other than grid or random search concepts, which are time consuming and computationally costly optimization algorithms. As a result, Bayesian optimization (Eriksson, Pearce et al. 2019), tree structured Parzen estimators (Zhao and Li 2018, Ozaki, Tanigaki et al. 2020), have been proposed to accelerate this process.

Here, we explore the effect of using different weight factors for the mean square error and thermodynamic constraints in order to generate normal and shear traction surfaces for a silicon/epoxy interface by employing mixed-mode fracture data generated by Wu et al. (2019). Metrics are established to demonstrate the effectiveness of Bayesian optimization in generating traction surfaces that retain the fidelity of the input data, while satisfying the selected thermodynamic consistency constraints.

The remainder of this paper is organized as follows. The theoretical underpinnings of our work are presented in Section 2. These are then implemented (Section 3) in the construction of a TCNN

that incorporates three thermodynamic constraints and Bayesian optimization algorithms. The results are presented and discussed in Section 4 and conclusions can be found in Section 5. Detailed derivations, supplementary figures and tables are included as Supplementary Information at the end of the manuscript.

## 2. Traction-separation relations and thermodynamic consistency

### 2.1 Interfacial traction separation relations

For a two-layer structure undergoing interfacial fracture as shown in Figure 1a, tractions are provided by a cohesive layer between the two substrates. This cohesive layer does not have a thickness *per se* and is assumed to be homogeneous<sup>1</sup>, which enables us to consider it as an assembly of identical springs connecting the two layers. The interfacial fracture process is then reproduced by the elongation and failure process of each spring along the interface. As shown in Figure 1a-b, for a stretched spring connecting the upper and lower layer, the normal and tangential tractions ( $\sigma_n, \sigma_t$ ) change with the normal and tangential separations ( $\delta_n, \delta_t$ ), which are defined by the change of the relative distances between the end points of the spring. Depending on the loading and boundary conditions, the ratio between the tangential and normal separations (i.e., the fracture mode-mix) varies. To quantitatively describe this relation, the vectorial separation is defined as the Euclidean norm,  $|\delta|$ , of the normal and tangential separation components. The mode-mix is represented by the phase angle,  $\phi$ , which is defined as the arctangent of the ratio between normal and tangential separations. Similarly, the vectorial traction is defined as  $|\sigma|$ . Thus

$$|\delta| = \sqrt{\delta_n^2 + \delta_t^2}, \quad (1a)$$

$$\phi = \text{atan}\left(\frac{\delta_t}{\delta_n}\right), \quad (1b)$$

$$|\sigma| = \sqrt{\sigma_n^2 + \sigma_t^2}. \quad (1c)$$

---

<sup>1</sup> Note that this assumption is not required for the general framework that is being developed here. However it was the case in the data that will be used as input for the neural network.

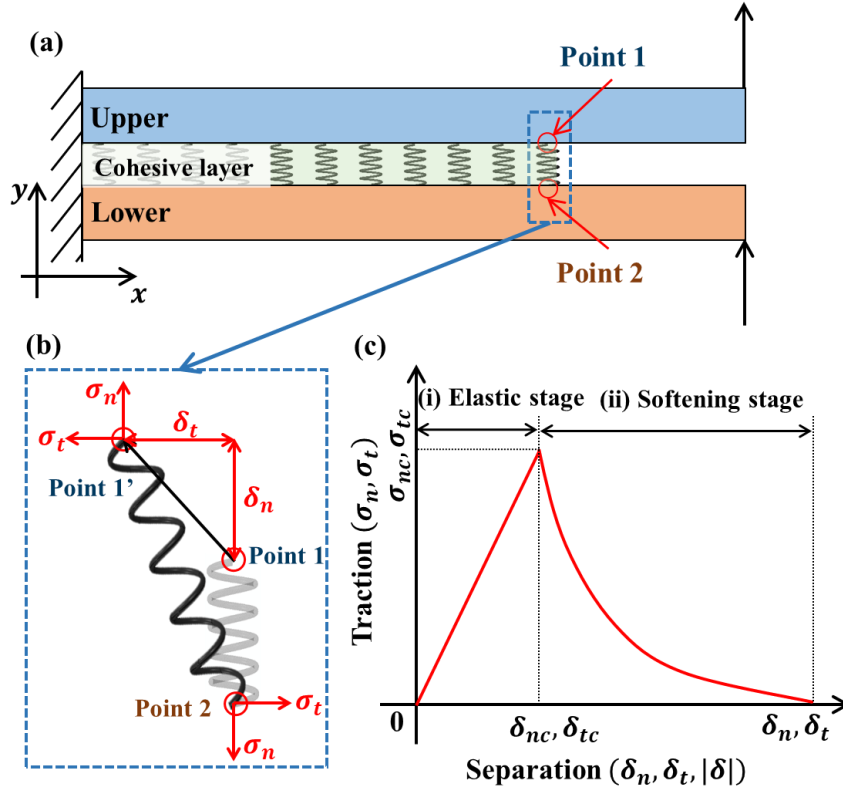


Figure 1: (a) Schematic of the specimen in an end loaded split experiment. (b) Tractions and separations for one spring. (c) A typical traction-separation relation with a two-stage response.

Traction-separation relations are the continuum representation of interfacial interactions. The normal and shear tractions,  $\sigma_n(\delta_n, \delta_t)$  and  $\sigma_t(\delta_n, \delta_t)$ , respectively, on the interface are generally functions of the normal and tangential ( $\delta_n, \delta_t$ ) separations across the interface. Typically, a traction-separation relation has two stages: (i) the elastic stage during which the tractions increase along with the separations, and (ii) the softening stage where the tractions decrease as the separations continue to increase. An example of a traction-separation relation is shown in Figure 1c, where the elastic stage has a linear profile, and the softening stage follows an exponential one. To examine the features of traction-separation relation data in detail, we plot the mixed-mode traction-separation relations that were extracted for a silicon-epoxy interface (Wu, Huang et al. 2019) in Figure 2a-b. Notice that the data for both normal and tangential relations are not smooth. Sharp peaks or discontinuities in gradients are commonly observed as shown in Figure 2c-d. These features make it unlikely that traction-separation relations can be represented by smooth functions,



which are the hallmark of potential-based approaches (Volokh 2004, Park, Paulino et al. 2009, Park and Paulino 2013).

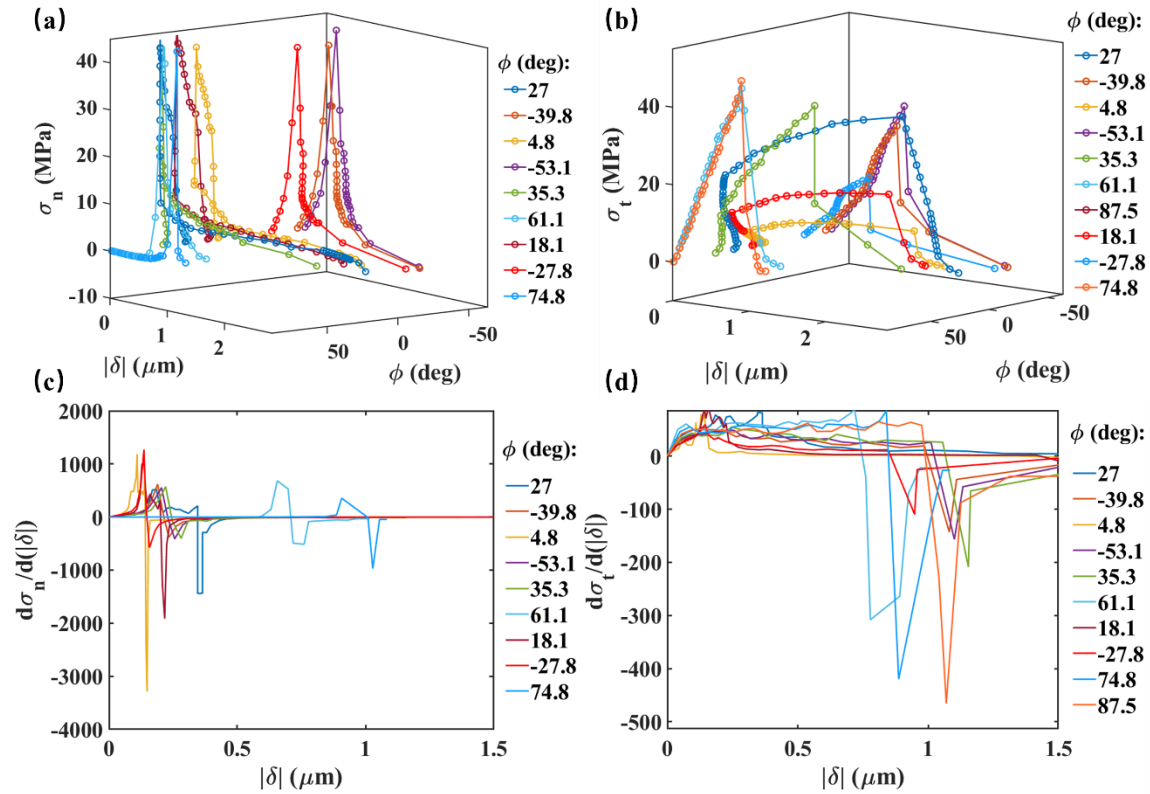


Figure 2. The (a) normal and (b) tangential components of the traction-separation relations for a silicon/epoxy interface in terms of total separation and phase angle. Gradient of (c) normal and (d) tangential tractions.

For instance, we explore the fitting of the experimental data with one of the most popular potential-based models: the Park, Paulino, and Roesler (PPR) model (Park, Paulino et al. 2009), which offers a large range of flexibility for modeling traction-separation relations using eight independent and adjustable parameters. The normalized modeling results are compared with the input experimental data in Figure 3. We note that the main inconsistency between the two is mainly due to the smoothness of traction-separation relations obtained by the PPR model in contrast to the pointed profile of the measured traction-separation relations. The fitting processes, which make use of Monte Carlo algorithms, are provided in Section S2 of the Supplementary Information. The gradient surfaces and curves along fixed phase angle loading paths are provided in Figures S1-S2.

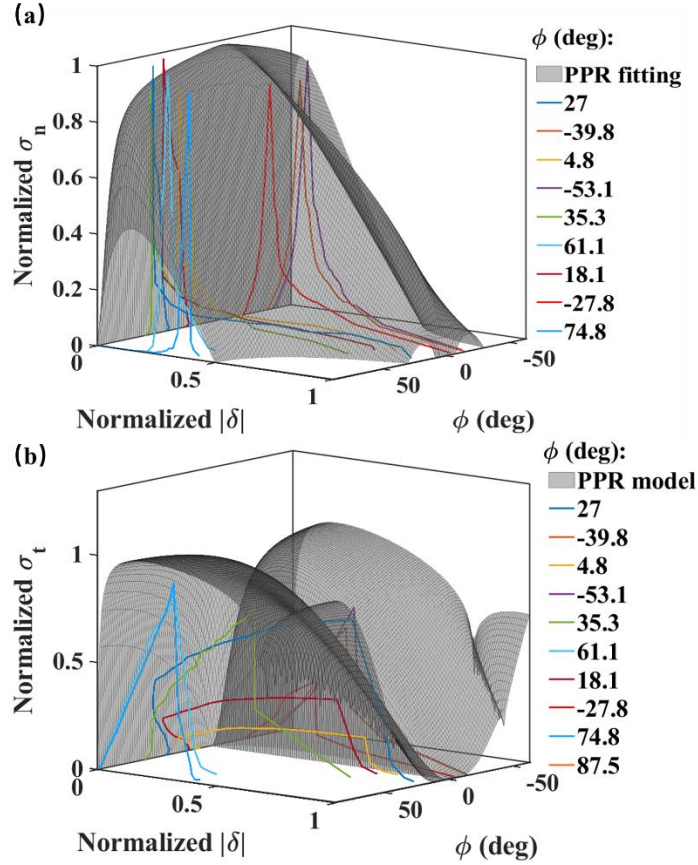


Figure 3. Normalized (a) normal and (b) tangential traction-separation surfaces that were fitted by the PPR model.

Certainly, there are other models (McGarry, Máirtín et al. 2014) that might provide better fits to the experimental data. However, we argue that these models would suffer the same challenges as the PPR model. This is due to a fundamental conflict between these theoretically conceived modeling approaches and the experimental data. The smoothness required in the selection of functional forms to describe the interfacial energy is such that it cannot fully capture all the features of the experimental data. Therefore, there is a need for the development of a data-driven approach that allows traction-separation relations to be directly modeled from experimental data in order to preserve the richness in the data sets, while simultaneously capturing the underlying laws of physics. Here we develop such an approach by combining deep neural networks with conditions for thermodynamic consistency.

## 2.2 Thermodynamic consistency

In this section we consider three conditions for thermodynamic consistency that the traction-separation surfaces obtained by deep neural networks should satisfy: (TC1), positive energy

dissipation; (TC2), maximum energy dissipation; and (TC3), conservation of the J-integral. Each of the three conditions are described, quantitatively defined, and prioritized based on certain features of the input data as well as other observations that are made from the experiments.

### 2.2.1 TC1: Positive energy dissipation

Fracture at interfaces is viewed as a process where the integrity of the interface is progressively lost due to the generation and propagation of defects, eventually yielding a fully cracked interface, as shown in Figure 4a. The degradation is characterized by energy dissipation and the accumulation of damage, which represented by a damage parameter,  $d$ , that ranges from 0 (intact interface) to 1 (complete failure) (Mosler and Scheider 2011, Lemaitre 2012). For monotonic loading, the energy dissipation for interfacial delamination is an irreversible process, i.e., positive energy dissipation, which also implies that the corresponding damage parameter (see Eq. 2 for definition) should be monotonically decreasing during the loading process. This thermodynamic consistency condition requirement can be therefore formulated as follows.

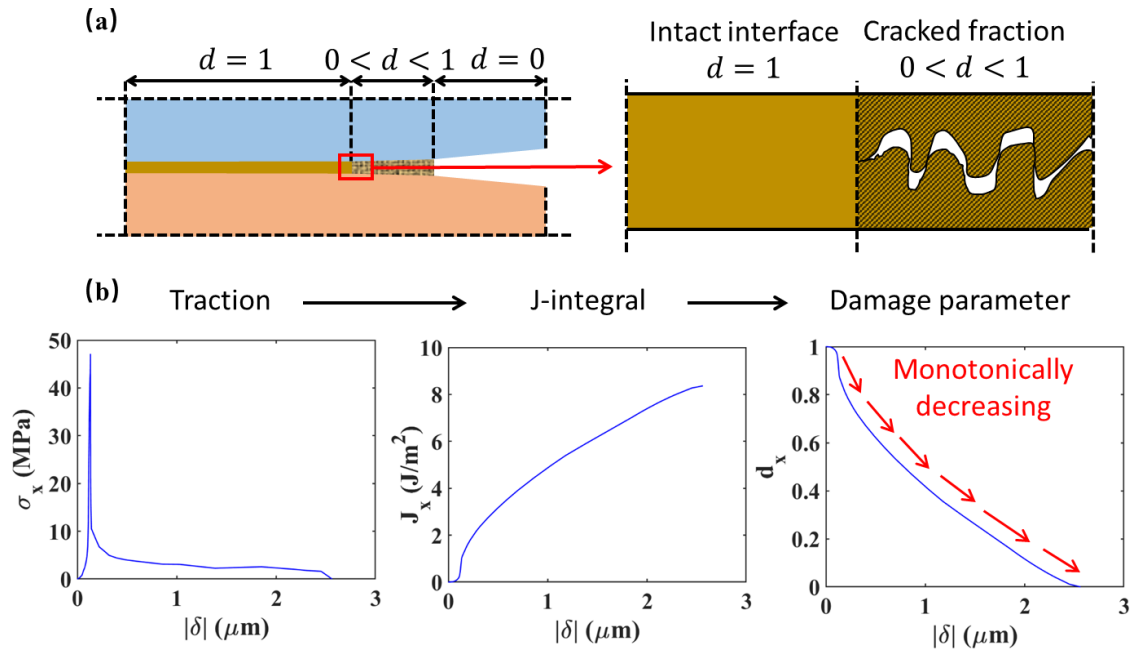


Figure 4. (a) Damage parameter of an interface. (b) Traction ( $\sigma_i$ , where  $(i = n, t)$  for normal or tangential) versus separation norm ( $|\delta|$ ), J-integral ( $J_i$ ) versus  $|\delta|$  and damage parameter ( $d_i$ ) versus  $|\delta|$ .

First, for an interface with pure mode I and mode II toughness values,  $\Gamma_I$  and  $\Gamma_{II}$ , respectively, the damage parameters for the normal and tangential directions ( $d_n$ ,  $d_t$ ) are defined based on the J-integrals and toughness,

$$d_n(\delta_n) = 1 - \frac{J_n(\delta_n)}{\Gamma_I}, \quad (2a)$$

$$d_t(\delta_t) = 1 - \frac{J_t(\delta_t)}{\Gamma_{II}}, \quad (2b)$$

where  $J_n$  and  $J_t$  are the normal and tangential components of the J-integral that are obtained by integrating tractions with respect to separation:

$$J_n(\delta_n) = \int_0^{\delta_n} \sigma_n(\delta_n) d\delta_n, \quad (3a)$$

$$J_t(\delta_t) = \int_0^{\delta_t} \sigma_t(\delta_t) d\delta_t. \quad (3b)$$

It should be noted here that the input data for the approach being proposed here came from mixed-mode fracture specimens that satisfied a balance condition (Wu, Huang et al. 2019) that allows the J-integral to be decoupled into its normal and tangential components, in spite of the fact that the traction-separation relations themselves may be coupled.

The positive energy dissipation condition can be fulfilled by enforcing a monotonically decreasing damage parameter along with positive dissipation (Clausius-Duhem inequality) as,

$$1 - \frac{\partial d_n}{\partial \delta_n} = \frac{\partial}{\partial \delta_n} \left( \frac{\int_0^{\delta_n} \sigma_n(x) dx}{\Gamma_n} \right) > 0, \quad (4a)$$

$$1 - \frac{\partial d_t}{\partial \delta_t} = \frac{\partial}{\partial \delta_t} \left( \frac{\int_0^{\delta_t} \sigma_t(x) dx}{\Gamma_t} \right) > 0, \quad (4b)$$

where  $\Gamma_I = \max(J_n)$  and  $\Gamma_{II} = \max(J_t)$ .

As an example, the normal components of the traction, J-integral, and damage parameter for an experimentally obtained traction-separation relation at a nominal phase angle of  $27^\circ$  are shown in Figure 4b. The calculated J-integral increases while the corresponding damage parameter decreases monotonically, indicating that this experimentally obtained traction-separation relation satisfies the monotonically positive energy dissipation condition.

### 2.2.2 TC2: Local steepest descent

In addition to the positive energy dissipation condition, the dissipation rate should reach a local maximum when the interfacial separation reaches a local maximum. For the damage parameter surface shown in Figure 5a, loading along fixed phase angle paths results in the largest separation change, making it the direction along which energy dissipation is fastest. For the point  $d_{n2}^{(i)}$ , loading

along a fixed phase angle path and moving to point  $d_{n2}^{(i+1)}$ , results in the largest decrease of the damage parameter compared with the neighboring points (e.g.,  $d_{n1}^{(i)}$  and  $d_{n3}^{(i)}$ ), where the phase angle does change. Here we define the loading angle as  $\theta = \tan^{-1} \left( \frac{d\phi}{d|\delta|} \right)$ , as shown in Figure 5b. The corresponding gradient along all directions is calculated and presented in Figure 5c. It shows that the gradient reaches its minimum when  $\theta$  reaches 0, which is also the direction of the maximum interfacial separation.

This local steepest descent condition (TC2 condition) is applied to damage associated with both the normal and tangential components of the traction-separation relations and can be described as follows,

$$\left( \frac{\partial d_n}{\partial \delta} \right)_{\theta=0} \leq \frac{\partial d_n}{\partial \delta} \text{ at any } \theta \quad (5a)$$

$$\left( \frac{\partial d_t}{\partial \delta} \right)_{\theta=0} \leq \frac{\partial d_t}{\partial \delta} \text{ at any } \theta \quad (5b)$$

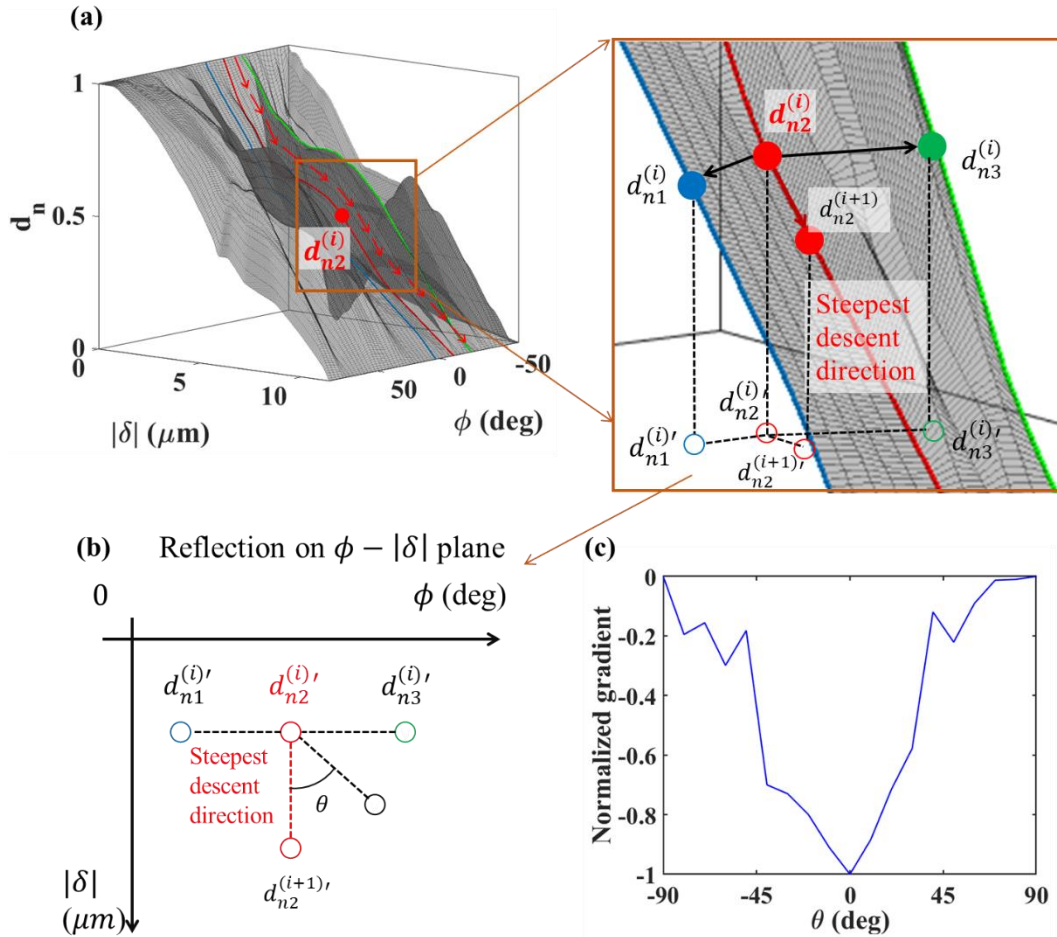


Figure 5. (a) Illustration of the local steepest descent condition. (b)  $\theta$  definition and (c) values of normalized gradient for any point (point  $d_{n2}^{(i)}$  as illustration) along all directions.

### 2.2.3 TC3: Conserving the J-integral

For interfacial failure processes, the total energy dissipation should equal the summation of the energy dissipation components along the normal and tangential separation directions if there is no other non-mechanical energy dissipation in the system (e.g., no heat generated from friction). For specimens that satisfy the balance condition and mixed-mode traction-separation relations along fixed phase angle loading paths, the total J-integral ( $J$ ) can be decomposed into its normal and tangential J-integral components, as shown in Figure 6,

$$J(\sigma_n, \sigma_t, \delta_n, \delta_t) = J_n(\sigma_n, \delta_n) + J_t(\sigma_t, \delta_t) \quad (6)$$

Under this circumstance, the normal and tangential separations increase proportionally with a ratio that is the tangent of the phase angle,

$$\frac{\delta_t}{\delta_n} = \tan \phi \quad (7)$$

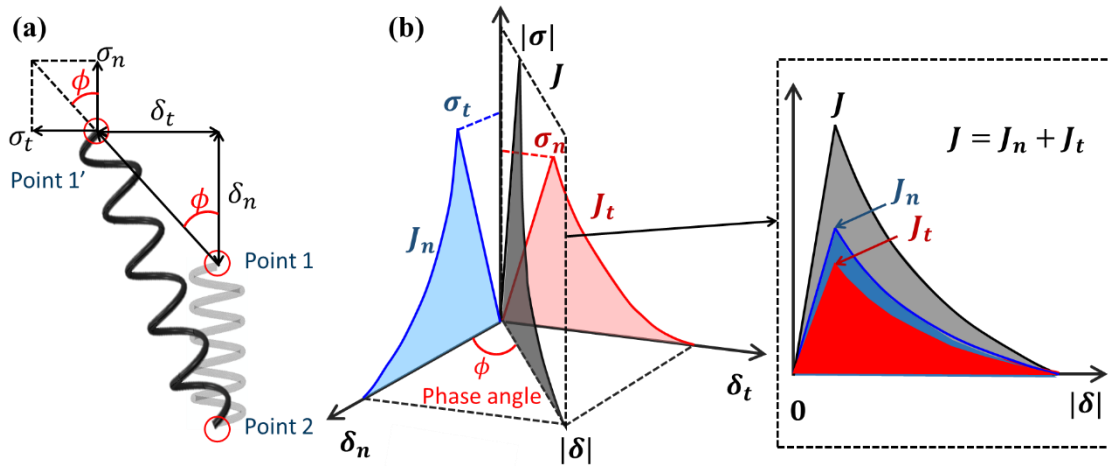


Figure 6. (a) Normal and tangential tractions and separations. (b) Conservation of the J-integral.

By replacing the normal and tangential J-integrals in Eq. 6 with integrals of tractions with respect to separations, the relation between normal and tangential tractions is obtained and expressed as follows:

$$\frac{\sigma_t}{\sigma_n} = \frac{\delta_t}{\delta_n} = \tan \phi . \quad (8)$$

This is the conservative loading path condition (TC3 condition) and its derivation from Eq. 6 can be found in Section S2 of Supplementary Information.

In reviewing all three TC conditions, it can be seen that TC1 and TC2 are developed based on the irreversible nature of energy dissipation as stated in the second law of thermodynamics. The third condition is based on the assumption that the delamination occurs at the interface in the absence of crack face contact and any resulting frictional energy dissipation. This is not always the case (Swadener, Liechti et al. 2002, Berggreen, Simonsen et al. 2007, Cordisco, Zavattieri et al. 2016), making this condition weaker than its first two counterparts.

### 3. Thermodynamically consistent neural network

In this section, we choose to work with a deep neural network to formulate a data-driven approach to develop surfaces for traction-separation relations based on a limited number of data sets corresponding to the loading paths that were taken in a series of mixed-mode fracture experiments. To include thermodynamically consistent conditions in this model, each of the conditions (TC1, TC2 and TC3) are embedded as loss function terms of the deep neural network to form the thermodynamically consistent neural network that is the basis of our approach. In addition, the importance of the experimental data and the thermodynamically consistent conditions are adjusted based on a Bayesian optimization algorithm, in order to balance any contradictions between experimental data and the thermodynamically consistent conditions.

#### 3.1 Deep neural network construction

We first constructed the deep neural network with two hidden layers and 60 neurons for each layer as shown in Figure 7. The inputs are the separation norm ( $|\delta|$ ) and phase angle ( $\phi$ ) as defined in Eq. 1a-b, whereas the outputs are the normal and tangential tractions ( $\sigma_n, \sigma_t$ ) (Figure 7).

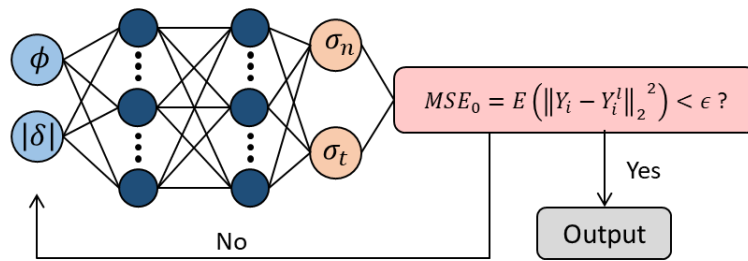


Figure 7. Deep neural network structure and optimization algorithm.

The input and output data are normalized by their maximum values in order to eliminate any bias introduced from relatively large difference in numerical values.

$$X_{norm}^{(i)} = \frac{X^{(i)}}{\max_{i \in [1, n]} X^{(i)}}, \quad (9a)$$

$$Y_{norm}^{(i)} = \frac{Y^{(i)}}{\max_{i \in [1, n]} Y^{(i)}}, \quad (9a)$$

where  $X^{(i)}$  and  $Y^{(i)}$  are the  $i^{\text{th}}$  values of the input and output data sets,  $n$  is the number of elements in the dataset and  $X_{norm}^{(i)}$  and  $Y_{norm}^{(i)}$  are the normalized data for training the deep neural network. We use the hyperbolic tangent function as the nonlinear activation function and the Adam optimizer that has been widely used as an effective and fast optimization method (Kingma and Ba 2014). The objective is to minimize the loss function that is embodied in the mean squared error and defined as:

$$MSE_0 = E \left( \|Y_i - Y_i^l\|_2^2 \right), \quad (10)$$

where  $Y_i$  and  $Y_i^l$  are  $i^{\text{th}}$  points, respectively, of the true and projected output. The operator  $\|\cdot\|$  represents the 2-dimensional Euclidean ( $l_2$ ) norm. The training process is complete when 1,000,000 training epochs (defined as the number of iterations during the training process) are reached, or the loss function value is smaller than a specific threshold, specified here as  $\epsilon = 10^{-3}$ . It should be noted that the number of training epochs (1,000,000) is determined by experience. At this stage, the deep neural network that incorporates the thermodynamic consistency conditions outlined here should be in a position to develop surfaces for mixed-mode traction-separation relations across a wide range of mode-mixes from a discrete number of experiments along proportional paths in mode-mix space.

### 3.2 Implementation

Thermodynamically consistent conditions are added to the loss function as penalty terms in the deep neural network, in order to increase its effectiveness and accuracy. In this approach, the training process is one that searches for a solution that represents the training data sets sufficiently well. The loss function, which includes the mean square error, is used to determine how well the fit is developing and then incorporates this information in optimization algorithms for any subsequent training steps. By implementing thermodynamic consistency conditions as terms in the loss function, any trained models that violate them are penalized while the surviving models are, by definition, in compliance. This concept has been implemented in physics informed (or guided) neural networks and has worked well in a number applications (Karpatne, Watkins et al. 2017, Raissi, Perdikaris et al. 2019, Yang and Perdikaris 2019).

In this work, each of the three thermodynamic consistency conditions are imposed on 10 loading paths along fixed phase angles ranging from  $-60^\circ$  to  $90^\circ$ , shown as the red lines in Figure



8, taken at equal increments of  $15^\circ$ . The interval along the  $|\delta|$  coordinate is set at  $0.1 \mu\text{m}$  within a range of  $[0, 3 \mu\text{m}]$ . We refer to these paths as constraining paths, to differentiate them from the experimental paths. For each iteration along each constraining path, the loss function value is calculated automatically based on predicted traction-separation relation surfaces. This value is then used to adjust the TCNN and move on to the next iteration.

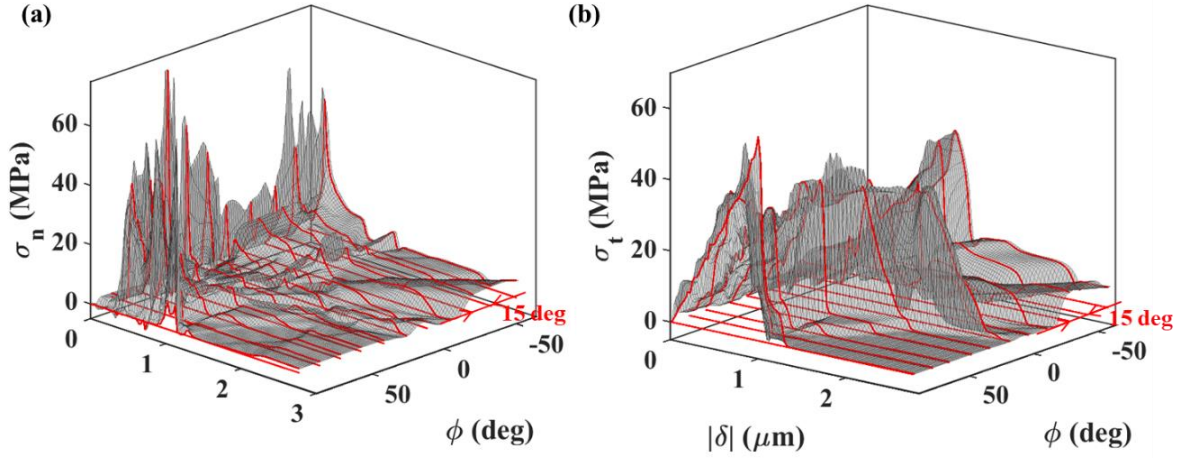


Figure 8. Illustration of fixed phase angle constraining paths on (a) normal and (b) tangential tractions.

### 3.2.1 Implementing the first thermodynamic constraint

The first thermodynamic consistency condition (TC1) is imposed on constraining paths on the surfaces of both the output normal and tangential components of the traction-separation relations. For each training epoch, the gradient of the damage parameter for each constraining path is calculated. The Max function is then used to compare these values with 0 so that only the positive part, which is contrary to the TC1 condition, is considered

$$MSE_{1n}^{(j)} = \max\left(\frac{\partial d_n}{\partial \delta_n}, 0\right) = \max_{i \in [1, n-1]} \left(\frac{d_n^{(i+1)} - d_n^{(i)}}{\delta_n^{(i+1)} - \delta_n^{(i)}}, 0\right), \quad (11a)$$

$$MSE_{1t}^{(j)} = \max\left(\frac{\partial d_t}{\partial \delta_t}, 0\right) = \max_{i \in [1, n-1]} \left(\frac{d_t^{(i+1)} - d_t^{(i)}}{\delta_t^{(i+1)} - \delta_t^{(i)}}, 0\right), \quad (11b)$$

where  $d_n^{(i)}$ ,  $d_t^{(i)}$  are the  $i^{\text{th}}$  normal and tangential damage parameters and  $\delta_n^{(i)}$ ,  $\delta_t^{(i)}$  are separations on  $j^{\text{th}}$  constraining path. The terms  $MSE_{1n}^{(j)}$  and  $MSE_{1t}^{(j)}$  are the normal and tangential components related to  $j^{\text{th}}$  constraining path and  $n$  is the total number of samples for each constraining path. Assuming that the normal and tangential damage parameters have the same weights, the new loss function ( $MSE_1$ ) that incorporates the first constraint is formulated as,

$$MSE_1 = \frac{1}{2m} \sum_{j=1}^m \left( MSE_{1n}^{(j)} + MSE_{1t}^{(j)} \right), \quad (12)$$

where  $m$  is the number of constraining paths. This loss function is averaged over the total number of points on the constraining paths.

### 3.2.2 Implementing the second thermodynamic constraint

The second thermodynamic consistency condition, TC2, (Eq. 5) constrains the gradient vector direction along proportional phase angle loading paths. Numerically, this condition is reflected as a smaller gradient along the  $|\delta|$  coordinate compared to the  $\phi$  coordinate. Along each constraining path, the difference between the gradients along the  $|\delta|$  and  $\phi$  directions are calculated and compared with value 0 using Max functions via:

$$MSE_{2n}^{(i,j)} = \max_{\substack{i \in [1, n-1] \\ j \in [2, m-1]}} \left( \frac{\partial d_n^{(i,j)}}{\partial(|\delta|)} - \frac{\partial d_n^{(i,j)}}{\partial \phi}, 0 \right) = \max_{\substack{i \in [1, n-1] \\ j \in [2, m-1]}} \left( \left( \frac{d_n^{(i,j)} - d_n^{(i+1,j)}}{\delta_n^{(i+1,j)} - \delta_n^{(i,j)}} \right) - \left( \frac{d_n^{(i,j)} - d_n^{(i,j+1)}}{\phi^{(i,j+1)} - \phi^{(i,j)}} \right), 0 \right) + \max_{\substack{i \in [1, n-1] \\ j \in [2, m-1]}} \left( \left( \frac{d_n^{(i,j)} - d_n^{(i+1,j)}}{\delta_n^{(i+1,j)} - \delta_n^{(i,j)}} \right) - \left( \frac{d_n^{(i,j)} - d_n^{(i,j-1)}}{\phi^{(i,j)} - \phi^{(i,j-1)}} \right), 0 \right) \quad (13a)$$

and

$$MSE_{2t}^{(i,j)} = \max_{\substack{i \in [1, n-1] \\ j \in [2, m-1]}} \left( \frac{\partial d_t^{(i,j)}}{\partial(|\delta|)} - \frac{\partial d_t^{(i,j)}}{\partial \phi}, 0 \right) = \max_{\substack{i \in [1, n-1] \\ j \in [2, m-1]}} \left( \left( \frac{d_t^{(i,j)} - d_t^{(i+1,j)}}{\delta_t^{(i+1,j)} - \delta_t^{(i,j)}} \right) - \left( \frac{d_t^{(i,j)} - d_t^{(i,j+1)}}{\phi^{(i,j+1)} - \phi^{(i,j)}} \right), 0 \right) + \max_{\substack{i \in [1, n-1] \\ j \in [2, m-1]}} \left( \left( \frac{d_t^{(i,j)} - d_t^{(i+1,j)}}{\delta_t^{(i+1,j)} - \delta_t^{(i,j)}} \right) - \left( \frac{d_t^{(i,j)} - d_t^{(i,j-1)}}{\phi^{(i,j)} - \phi^{(i,j-1)}} \right), 0 \right), \quad (13b)$$

where  $d_n^{(i,j)}$ ,  $d_t^{(i,j)}$  and  $\delta_n^{(i,j)}$ ,  $\delta_t^{(i,j)}$  are the  $i^{\text{th}}$  normal and tangential damage parameters as well as separations on  $j^{\text{th}}$  constraining path.  $MSE_{2n}^{(i,j)}$  and  $MSE_{2t}^{(i,j)}$  are the normal and tangential components related to  $i^{\text{th}}$  point on  $j^{\text{th}}$  constraining path of this loss function term.

For data points obeying the second condition, this difference is negative, and the corresponding loss function term yields 0. For contradicting data points, the loss function term is positive and is minimized during the training process.

These constraints are imposed separately on normal and tangential traction-separation relation surfaces and play an equally important role in the total loss function term ( $MSE_2$ ),

$$MSE_2 = \frac{1}{2mn} \left( \sum_{i=1}^{n-1} \sum_{j=2}^{m-1} MSE_{2n}^{(i,j)} + \sum_{i=1}^{n-1} \sum_{j=2}^{m-1} MSE_{2t}^{(i,j)} \right). \quad (14)$$

### 3.2.3 Implementing the third thermodynamic constraint

The third condition confines the ratio between the normal and tangential tractions to follow the constraining paths. The third loss function term ( $MSE_3$ ) for each constraining path is defined as:

$$MSE_3^{(j)} = \frac{1}{n} \sum_{i=1}^n \left| \left( \frac{\sigma_t^{(i,j)}}{\sigma_n^{(i,j)}} - \tan(\phi^{(j)}) \right) \right|. \quad (15)$$

The terms  $\sigma_n^{(i,j)}$ ,  $\sigma_t^{(i,j)}$  are the  $i^{\text{th}}$  normal and tangential tractions of  $j^{\text{th}}$  constraining path.  $MSE_3^{(j)}$  is the loss function related to the  $j^{\text{th}}$  constraining path. This constraint differs from the first two in that it is an equality as opposed to an inequality. The assembled total loss function ( $MSE_3$ ) term corresponding to the third constraint is written as:

$$MSE_3 = \frac{1}{m} \sum_{j=1}^m MSE_3^{(j)}. \quad (16)$$

#### 3.2.4 *Weighted loss functions for the thermodynamically consistent neural network*

The loss function terms with the conditions TC1-TC3 embodied as constraints (Eq. 12, 14, 16 respectively), are implemented in a deep neural network so as to construct a thermodynamically consistent neural network. The schematic for this network is shown in Figure 9. The deep neural network uses the same architecture as was discussed in Section 3.1: it has two hidden layers with 60 neurons for each hidden layer.

Different weight factors  $\lambda_i$  were considered in order to investigate the effect of the imposed thermodynamically consistent constraints on the performance of the proposed neural network. Three different thermodynamically consistent neural networks (designated TCNN1 to TCNN3) were compared by considering three sets of weight factors. The active constraints and weight factors for all three sets are listed in Table. 1, bearing in mind that  $\sum_{i=0}^3 \lambda_i = 1$ .

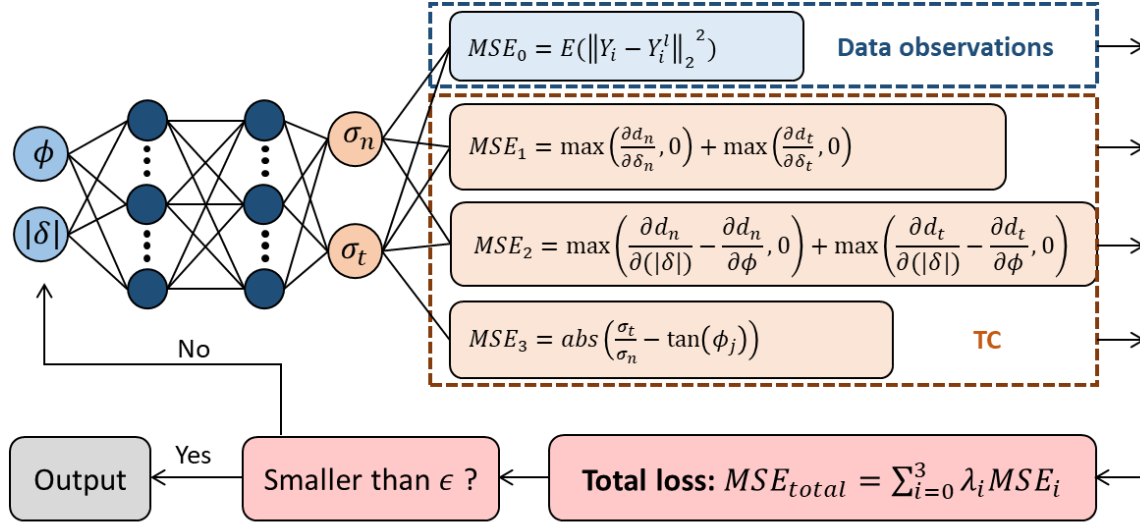


Figure 9. Schematic of a thermodynamically consistent neural network for developing surfaces for

Table. 1 Weight factor setting

	$\lambda_0$	$\lambda_1$	$\lambda_2$	$\lambda_3$	Active TC constraints
TCNN1	0.800	0.200	0.000	0.000	TC1
TCNN2	0.600	0.200	0.200	0.000	TC1, TC2
TCNN3	0.570	0.200	0.200	0.0300	TC1, TC2, TC3

From TCNN1 to TCNN3, the weight factor for  $MSE_0$  term ( $\lambda_0$ ) is reduced and redistributed to the thermodynamic consistency conditions step by step. An accurate fitting to the traction-separation relations along the paths taken in the series of experiments was still given the highest priority. This meant that  $\lambda_0$  was always greater than 0.5 in order to ensure that the main features of the data from the experiments were captured. The constraints TC1 and TC2 were treated with equal importance and thus were assigned the same weight factor. Being an equality, the third constraint is inherently stronger than the inequalities that are embodied in the first two constraints. If all three constraints are assigned the same weight factor, the third one would therefore dominate the process. Accordingly,  $\lambda_3$  was assigned smaller values in order to balance the contribution from each of the three constraints.

### 3.3 Bayesian optimization

In the previous section, the certain weight factors were selected in order to demonstrate their effect in a limited manner. This raises a question as to what the best rationale is for selecting the various weight factors. Here we selected Bayesian optimization (Snoek, Larochelle et al. 2012, Shahriari, Swersky et al. 2015) to automatically adjust the weight factors, so that the relative importance of mean square error and thermodynamic consistency terms are optimized, and a minimum total loss function can be reached.

In many cases, experimental data is accompanied by systematic errors and noise, which can lead to localized conflict between experimental results and thermodynamic consistency conditions. When used as training data sets in the TCNN models, these factors can significantly affect the projected traction-separation surfaces and lead to portions of the surfaces that violate thermodynamic consistency. Moreover, this conflict can interfere with the training processes within the TCNN, which can result in issues such as excessive training for convergence or poor representations of the experimental data. By using automatically selected weight factor adjustment algorithms for optimization, a minimum loss function value can be reached in an optimal manner. As a result, the projection of traction-separation relations may adjust portions of the input data in order to satisfy thermodynamic consistency when conflicts are identified, while still capturing the main features of the input data.

The Bayesian optimization algorithm that performs global minimization of unknown functions with multiple degrees of freedom (Snoek, Larochelle et al. 2012, Shahriari, Swersky et al. 2015), is adopted for the optimization. Using knowledge obtained from some prior sampling over the space of this unknown function, the Bayesian optimization algorithm estimates the areas with highest possibility to generate most promising results. In this way, instead of conducting random or grid searches where results should be obtained for every set of parameters, the Bayesian optimization algorithm provides more optimal searches and reduces the number of trial attempts by taking advantage of prior knowledge and the calculated likelihood of the unknown area. Our implementation is conducted within the confines of the Trust-region Bayesian optimization (TuRBO) algorithm (Eriksson, Pearce et al. 2019), which solves for global optimization of large-scale high-dimensional problems using a local probabilistic approach.

In integrating the Bayesian optimization algorithm with the TCNN described earlier, the set of the weight factors is determined such that it minimizes the overall loss function value while the following actions are taken: (1) the weight factors for all terms in the loss function are relaxed and

allowed to vary within a reasonable range; (2) the values of the weight factors used in TCNN3 were upper bounds for those selected in the optimization process.

The implementation of TCNN framework with Bayesian optimization is shown in Figure 10 with the following steps.

Step 1. The normalized training data and the randomly initiated weight factors are input for the first training step.

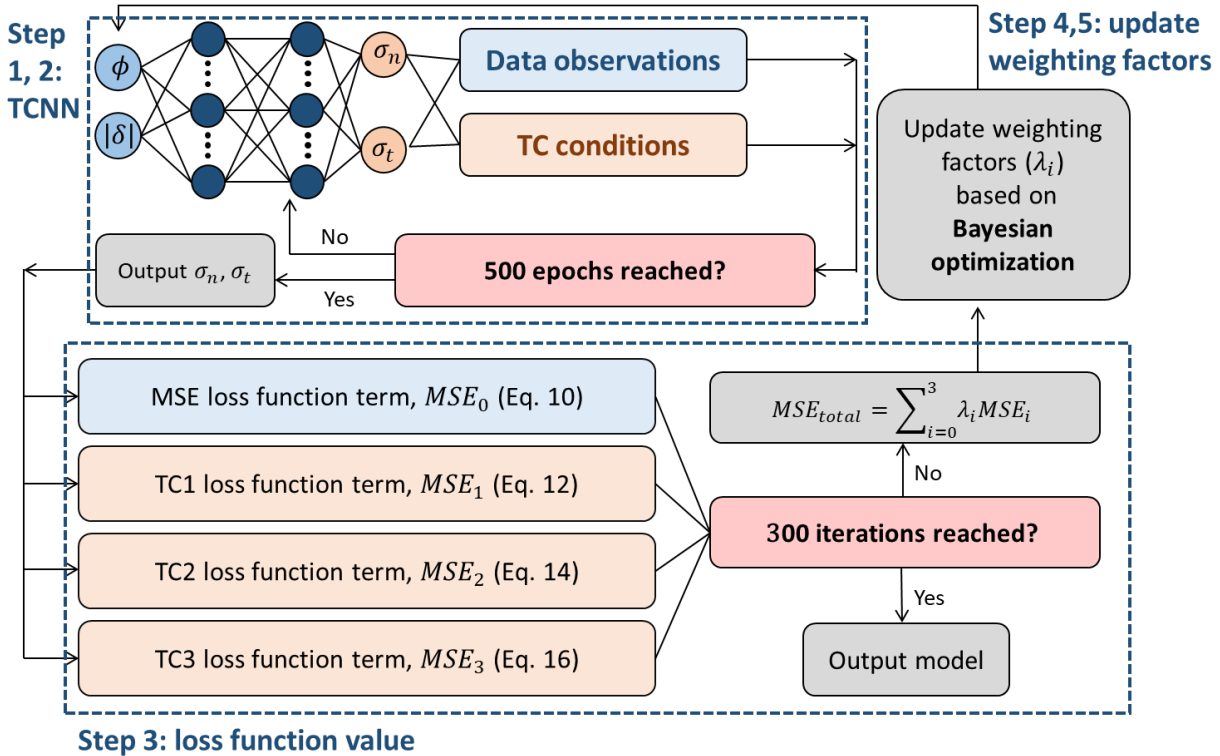


Figure 10. Bayesian optimization of weight factors.

Step 2. TCNN is trained for 500 epochs; this relatively low epoch number reduces the time required for each iteration of the Bayesian optimization.

Step 3. Upon the completion of the TCNN training process, values of loss function terms corresponding to MSE (based on Eq. 10) and TC1-3 conditions (based on Eq. 12, Eq. 14 and Eq. 16) are calculated. The total loss function value is then obtained from Eq. 17.

Step 4. The weight factors are updated based on Bayesian optimization criteria.

Step 5. The updated weight factors are input to the TCNN to start the next iteration. This cycle continues until the maximum budget (300 iterations, determined by experience) is reached.

For each iteration in the Bayesian optimization algorithm, the weight factors are optimized under two constraints: (1) Each weight factor varies within a range defined by lower and upper

bounds ( $\lambda_i \in [\lambda_i^{lower}, \lambda_i^{upper}]$ ,  $i = 0, 1, 2$  or  $3$ ). This allows the user to rank the constraints while avoiding weight factors that are smaller than zero. (2) The weight factors must satisfy the condition  $\sum_{i=0}^3 \lambda_i = 1$ . The updated weight factor set is transferred to the TCNN for the next training step. The end of the optimization process is reached when the maximum number (e.g., 300, determined by experience) of iterations is reached.

## **4. Results and Discussion**

As a basis for discussion of the results obtained from the ideas presented above, we first obtained the surfaces for mixed-mode traction-separation relations using a deep neural network without any constraints. Subsequently, we discuss the improvements that can be obtained by adding thermodynamic constraints with three sets of selected weight factors and then demonstrate the effectiveness of the weight factors selected by the Bayesian optimization algorithm.

### **4.1 Deep Neural Network**

The normal and tangential traction-separation relation surfaces obtained from only using the basic deep neural network are illustrated (Figure 11a-b) with respect to  $|\delta|$  and  $\phi$ . The traction-separation relations that are embodied in the result were extracted and are compared (Figure 11c-d) with the input data sets along the various loading paths that were considered in the experiments. It can be seen that the agreement was quite reasonable.

We then evaluated how thermodynamically consistent the result was. Based on the surfaces for traction-separation relations that were obtained with thermodynamic constraints incorporated in the deep neural network, violations to each of the three thermodynamically consistent conditions are calculated separately as follows:

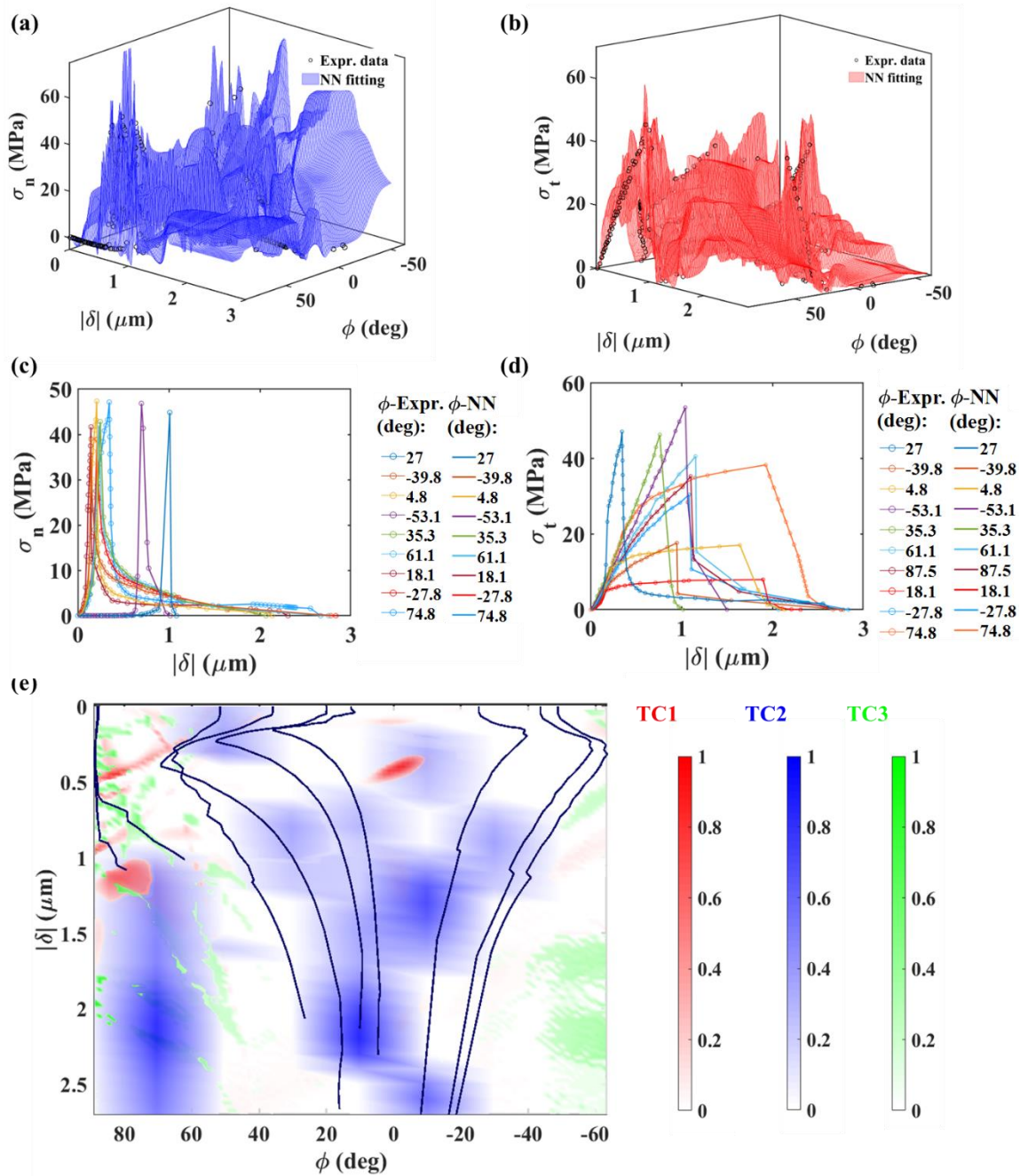


Figure 11. (a) Normal and (b) tangential traction surfaces obtained using the deep neural network by itself without any constraints. Comparison with (c) normal and (d) tangential tractions obtained experimentally at specific mode-mixes. (e) Violations associated with each of the three thermodynamically consistent conditions: The red, blue and green contours represent the degrees of violation of conditions TC1, TC2 and TC3 respectively, while the black lines are the loading paths that were taken in the experiments.



For the TC1 condition, we introduce the violation term, ( $\text{Vio}_1$ ), which represents negative energy dissipation and was calculated based on gradient of the J-integrals calculated from the predicted values of the tractions from

$$\text{Vio}_1 = \left| \min \left( \frac{\partial J_n}{\partial |\delta|}, 0 \right) \right| + \left| \min \left( \frac{\partial J_t}{\partial |\delta|}, 0 \right) \right|. \quad (18)$$

This equation is used to identify data points that have a negative gradient of the J-integral components. Their normalized values ( $\overline{\text{Vio}}_1$ ), with respect to the maximum value

$$\overline{\text{Vio}}_1 = \frac{\text{Vio}_1}{\max(\text{Vio}_1)} \quad (19)$$

are illustrated as the red contour in Figure 11e.

For the TC2 condition, the damage surfaces are first calculated automatically based on predicted traction-separation relations for each iteration (defined in Eq. 2). The gradient change is then calculated with respect to loading angle,  $\theta$ , for each point of the damage surface as shown in Figures 5b-c. Data points with maximum gradient decreases that are not along the  $\theta = 0^\circ$  direction are located and the violation ( $\text{Vio}_2$ ) is calculated as the difference between the fastest descending direction and  $0^\circ$ , as shown in following equation.

$$\text{Vio}_2 = |\theta_{adn}| + |\theta_{dat}|, \quad (20)$$

where  $\theta_{adn}$  and  $\theta_{dat}$  are the angle of fastest descending direction in the normal and tangential traction-separation relation surfaces. The normalized value ( $\overline{\text{Vio}}_2$ ) is taken to be

$$\overline{\text{Vio}}_2 = \frac{\text{Vio}_2}{\max(\text{Vio}_2)} \quad (21)$$

with respect to maximum value and is shown as the blue contour in Figure 11e.

For the final condition (TC3), the ratio between the normal and tangential tractions ( $\sigma_n, \sigma_t$ ) is calculated and compared with the tangent of the phase angle,  $\phi$ . Noting that exact equivalence is usually impossible to achieve, we use a threshold angle ( $\epsilon_{phi}$ ) of  $5^\circ$  and violation ( $\text{Vio}_3$ ) is reached when the difference between the ratio and the phase angle tangent is larger than  $\epsilon_{phi}$ : Thus

$$\text{Vio}_3 = \max \left( \left| \frac{\sigma_t}{\sigma_n} - \tan \phi \right|, \tan(\epsilon_{phi}) \right) - \tan(\epsilon_{phi}) \quad (22)$$

Again, a normalized value ( $\overline{\text{Vio}}_3$ )

$$\overline{\text{Vio}}_3 = \frac{\text{Vio}_3}{\max(\text{Vio}_3)}, \quad (23)$$

is introduced and then depicted as the green contour shown in Figure 11e.

It can be seen that a significant portion of the violation map (Figure 11e) is colored, indicating that there is a substantial degree of violation in the traction-separation relation surfaces that are produced by the deep neural network operating in the absence of any constraints. The strongest thermodynamic consistency condition (TC1, red) was violated over relatively small portions of the surfaces. In addition, none of the loading paths taken in the experiments violated this condition. There are a lot of blue regions in the map corresponding to areas on the surfaces where the second consistency condition is violated. In addition, a number of the loading paths taken in the experiments pass through these regions, suggesting that enforcing this condition in the learning process will be helpful. Finally, the region where the third condition is violated is relatively small, making this a candidate for a relatively low weight factor.

#### **4.2 Thermodynamically consistent deep neural network (TCNN)**

The effect of the different weight factors (Table 1) that were applied to each of the thermodynamically consistency conditions is illustrated in Figures 12-14, corresponding to TCNN1 to TCNN3, respectively.

What can be learned by comparing the results from Figures 12-14? First, it can be seen (sub-Figures c-d) that the surfaces produced by all three cases that were considered here compared well with the input data from the experiments. Thus, the main features of the input data are captured in the training process. Shifting our focus to the degree of violation (sub-Figure e) of each of the conditions, it is clear that adding the constraints reduced the amount of violation compared to the simple neural network (Figure 11e). Furthermore, the amount of overlap between violations decreased as more constraints were added. Nonetheless, even for the best combination of weight factors considered here (TCNN3), portions of the loading paths were still in violation. This suggests that systematic errors and noise in the experimental data lead to violations and provides an opportunity to improve certain aspects of the data, particularly if the main contributors can be identified. Another thing to consider is that the examples provided in this section are only three of a potentially infinite number of combinations of weight factors. The next section presents the results of the Bayesian optimization approach (Section 3.3) to optimizing the selection of weight factors.

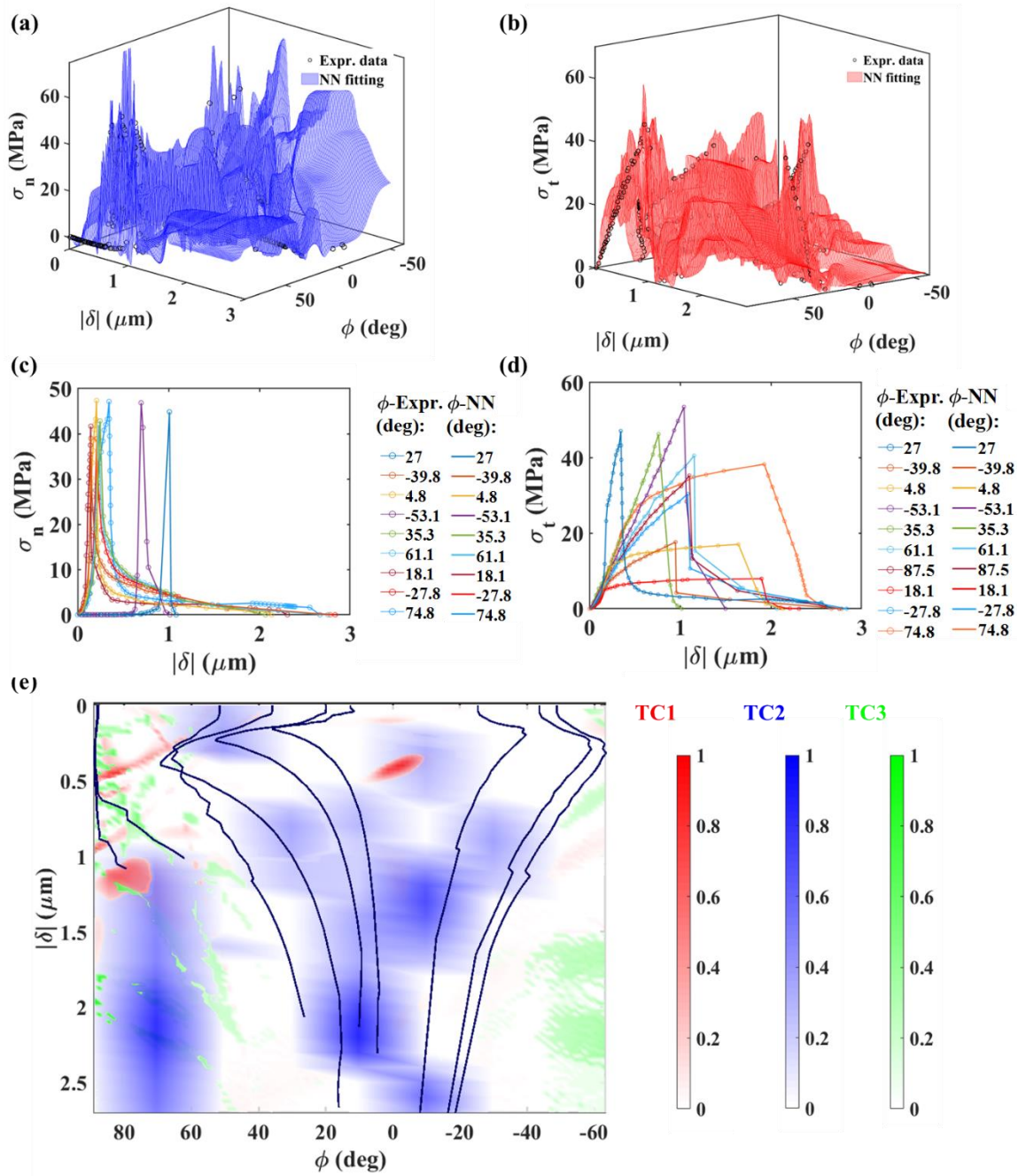


Figure 12. Results for the TCNN operating with MSE ( $\lambda_0 = 0.8$ ) and only the TC1 constraint ( $\lambda_1 = 0.2$ ): Surfaces for (a) normal and (b) tangential tractions; comparing results for (c) normal and (d) tangential tractions with those from experiments. (e) Violations associated with each of the three thermodynamically consistent conditions: The red, blue and green contours represent the

degrees of violation of conditions TC1, TC2 and TC3 respectively, while the black lines are the loading paths that were taken in the experiments.

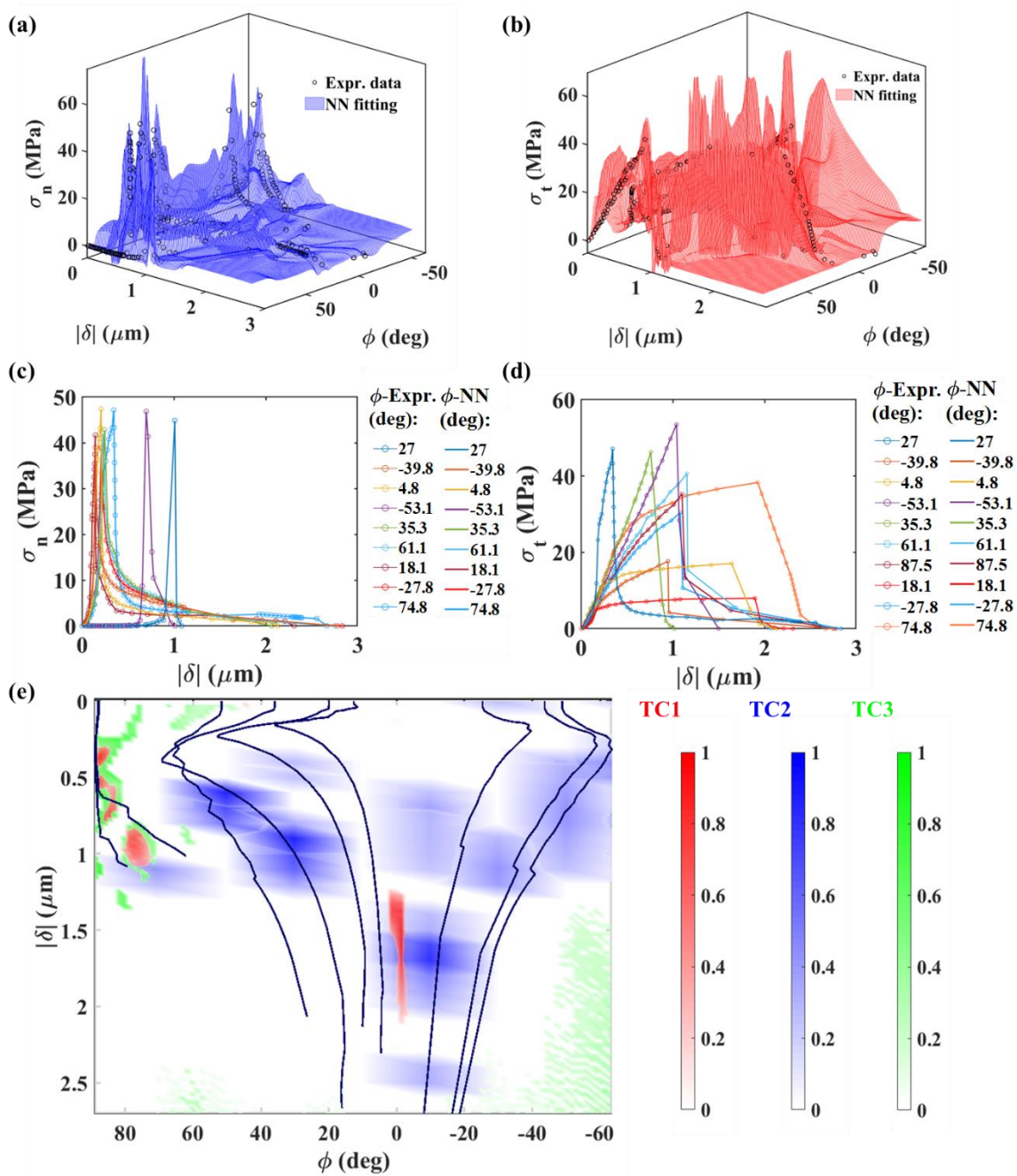


Figure 13. Results for the TCNN operating with MSE ( $\lambda_0 = 0.6$ ) and the conditions TC1 and TC2 ( $\lambda_1 = 0.2, \lambda_2 = 0.2$ ): Surfaces for (a) normal and (b) tangential tractions; comparing results for (c)

normal and (d) tangential tractions with those from experiments. (e) Violations associated with each of the three thermodynamically consistent conditions: The red, blue and green contours represent the degrees of violation of conditions TC1, TC2 and TC3 respectively, while the black lines are the loading paths that were taken in the experiments.

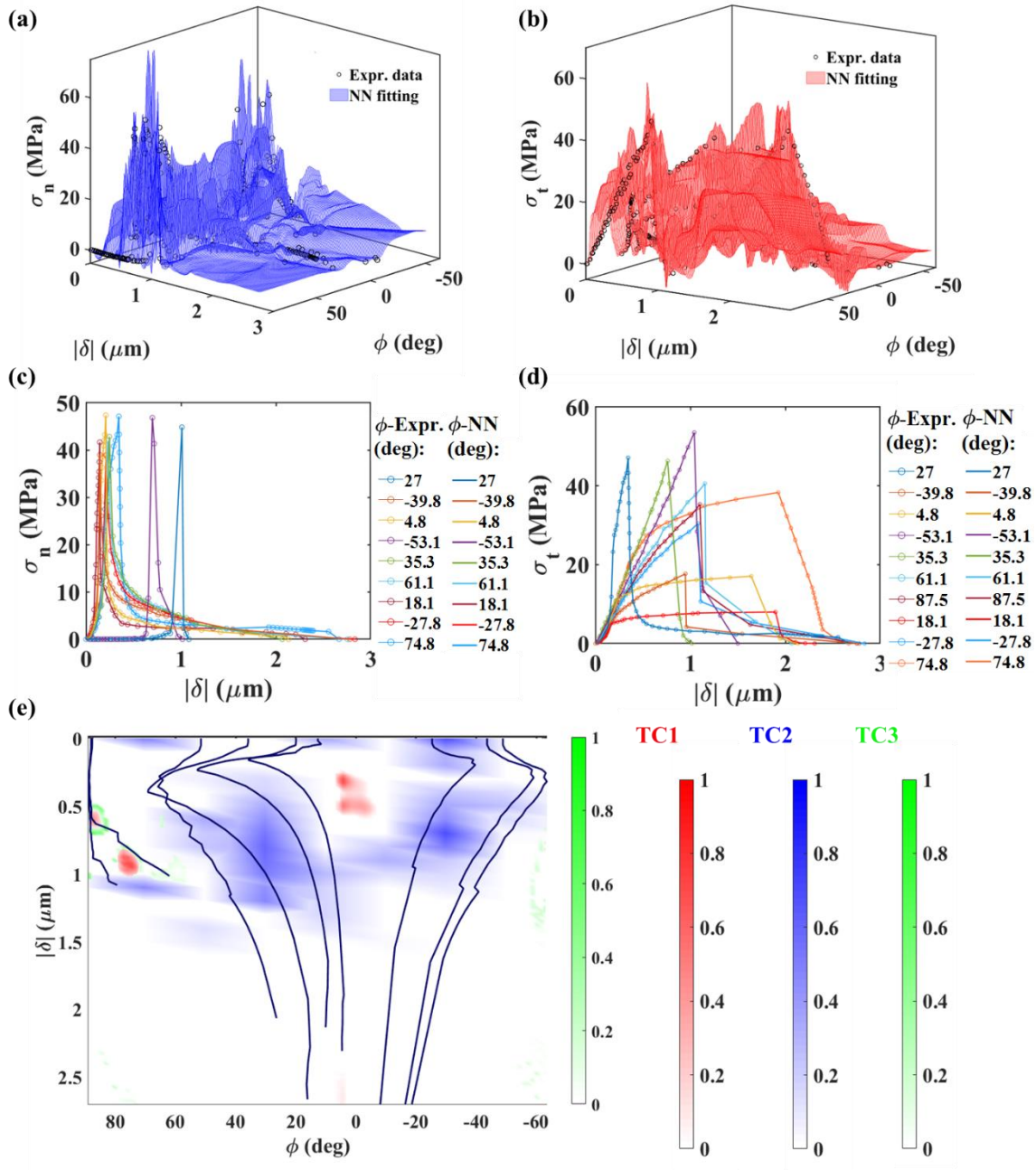


Figure 14. Results for the TCNN operating with MSE ( $\lambda_0 = 0.57$ ) and the conditions TC1 and TC2 ( $\lambda_1 = 0.2, \lambda_2 = 0.2, \lambda_3 = 0.03$ ): Surfaces for (a) normal and (b) tangential tractions; comparing

results for (c) normal and (d) tangential tractions with those from experiments. (e) Violations associated with each of the three thermodynamically consistent conditions: The red, blue and green contours represent the degrees of violation of conditions TC1, TC2 and TC3 respectively, while the black lines are the loading paths that were taken in the experiments.

### 4.3 Bayesian optimization of weight factors

Based on the Bayesian optimization algorithm proposed in Section 3.3, the weight factors for loss function terms corresponding to the MSE as well as the thermodynamic consistency conditions (TC1-TC3) are optimized. The convergence of the process is shown in Figure 15 after 300 iterations were conducted. The value of the loss function initially decreases rapidly, reducing to approximately 1.0 within 25 iterations. The decrease in the values of the loss function beyond that follows a quasi-exponential form with small fluctuations. Ranges for each of the four weight factors ( $\lambda_0 - \lambda_3$ ) and their optimized values are presented in Table 2. It can be seen that the largest importance is still awarded to the data from the experiments (MSE,  $\lambda_0 = 0.519$ ). Second priority was given to the second law of thermodynamics (TC1,  $\lambda_1 = 0.385$ ) and it was obeyed by all the input data sets. The weight factor associated with the second thermodynamic constraint was considerably lower ( $\lambda_2 = 0.0622$ ) than the lowest value (0.2) that was used in the three examples described earlier. One possible explanation is that other energy dissipation mechanisms, e.g., friction, may be involved when the loading directions are changed. This is also reflected as the larger blue areas in Figures 12-14e. The optimized weight factor for the third condition (TC3,  $\lambda_3 = 0.0388$ ) is close to the setting that was used in TCNN3 settings, maintaining the position of this constraint as the lowest in importance.

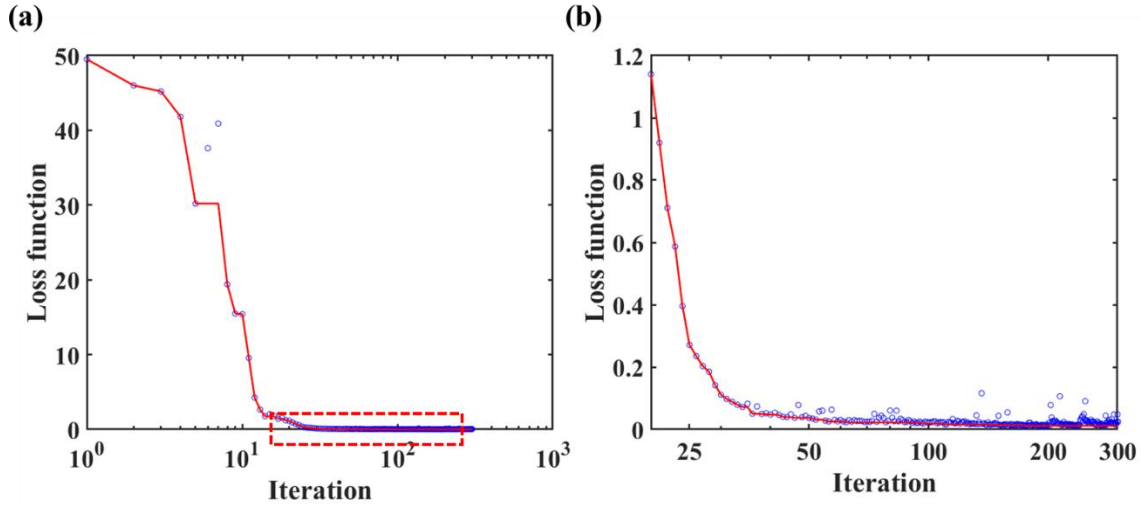


Figure 15. (a) Convergence of the Bayesian optimization process for optimizing the values of the weight factors. (b) Enlarged image for region within the dashed red frame in (a).

Table. 2 Optimized Weight Factors

	Upper bound	Lower bound	Optimized
$\lambda_0$ (MSE)	0.750	0.400	0.519
$\lambda_1$ (TC1)	$(1 - \lambda_0) \times 0.900$	$(1 - \lambda_0) \times 0.100$	0.385
$\lambda_2$ (TC2)	$(1 - \lambda_0 - \lambda_1) \times 0.900$	$(1 - \lambda_0 - \lambda_1) \times 0.100$	0.0622
$\lambda_3$ (TC3)	NA	NA	0.0338

We used Figures 11-14 to illustrate the effect of various combinations of weight factors, so it is now instructive to return to that format in Figure 16 to observe the effect of the optimized selection of weight factors. The resultant traction surfaces are shown in Figure 16a-b. These are the surfaces that would be used in cohesive zone modelling of crack initiation and growth in structures such as microelectronics packages that contain silicon/epoxy (e.g., molding compound) interfaces. The veracity of these surfaces is first observed in Figure 16c-d, where the optimized neural network approach maintains good correspondence with the input experimental data even though the MSE weight factor was reduced to 0.519 from 0.570, the lowest value that was used in our initial trials.

Compared to the results shown in Figure 14e, Bayesian optimization, which also applied all three constraints, significantly reduced the degree of violation (Figure 16e). Furthermore, it can be

seen that now only very small portions of the loading paths that were taken in the experiments are in violation of any of the three constraints. Thus, Bayesian optimization has effectively reduced the degree of conflict between the thermodynamic constraints and the input data. The trend of the experimental data is still fully captured while sufficiently honoring all three thermodynamic constraints. The Bayesian optimization also confirms that the third constraint (TC3) is the least important one.



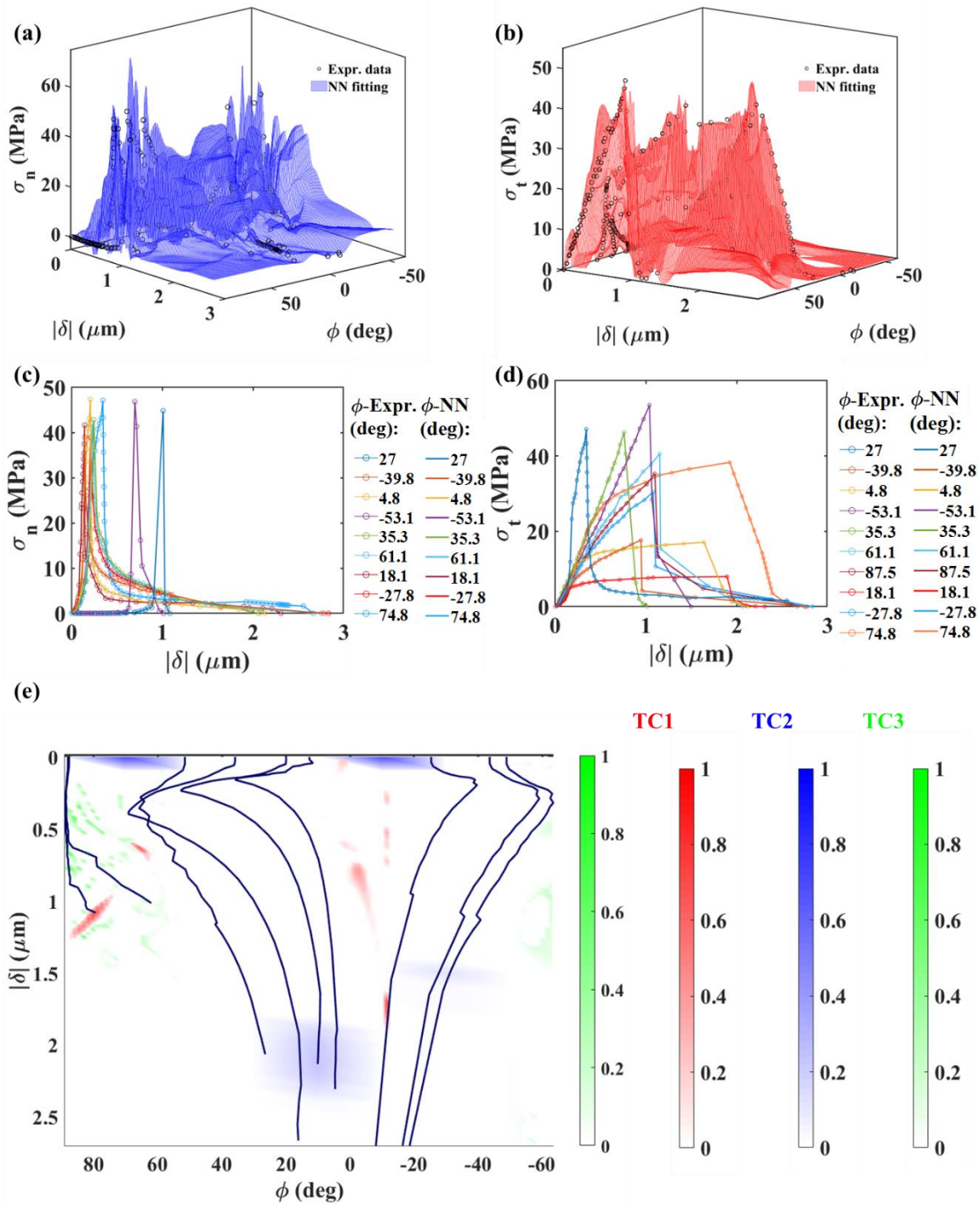


Figure 16. Results for the TCNN with Bayesian optimization. Surfaces for (a) normal and (b) tangential tractions; comparing results for (c) normal and (d) tangential tractions with those from experiments. (e) Violations associated with each of the three thermodynamically consistent conditions: The red, blue and green contours represent the degrees of violation of conditions TC1,

TC2 and TC3 respectively, while the black lines are the loading paths that were taken in the experiments.

#### 4.4 Fitting errors and constraint violations

The evaluation of the error and degree of violation of constraints that was presented in Figures 11-14c-e and 16c-e can be made more quantitative by introducing the fitting error and violation rate. The fitting error is defined as:

$$\text{Fitting error} = \text{Es} \left( \|Y_i - Y_i^l\|_2^2 \right), \quad (24)$$

where  $Y_i$  and  $Y_i^l$  are, respectively, the  $i^{\text{th}}$  value of the input data and predicted output along the loading paths that were taken in the experiments.

The degree of violation of the thermodynamic constraints is defined on the basis of the regions where violations occurred in Figures 11-14e and 16e and is given by:

$$\text{Violation ratio} = \frac{A_V}{A_M}, \quad (25)$$

where  $A_V$  is the area where violations occurred and  $A_M$  is the total area of region that was modelled. The results are shown in Figure 17 for all the cases that have been considered here, from the basic neural network approach to the one that introduced Bayesian optimization.

Interestingly the deep neural network, operating without any constraints, provided the smallest fitting error (Figure 17a). Furthermore, the neural network that introduced thermodynamic constraints via Bayesian optimization produced the largest fitting error. Nonetheless, all fitting errors were less than 5%, indicating that the input data was sufficiently well-learned by all five approaches.

By contrast (Figure 17b), the deep neural network operating by itself, without any constraints, had the highest violation ratio of all the approaches that were considered here. The violation rate across all three constraints was almost 60%, with most of that coming from the second constraint (TC2). As expected, this situation is significantly improved when the thermodynamic constraints were introduced as terms in the loss function. The first set of weight factors, which were directed at the first thermodynamic constraint, resulted in a significant reduction in its violation ratio, which had to be relaxed as the other constraints were introduced. This was due to the noise and systematic errors in the experiments, which induced conflict additional conflict with the thermodynamic constraints. This conflict was mediated by introducing Bayesian optimization, which was able to

strike a balance between capturing the main trend of the experimental data while bypassing the conflicts that are introduced by uncertainties in the experiments.

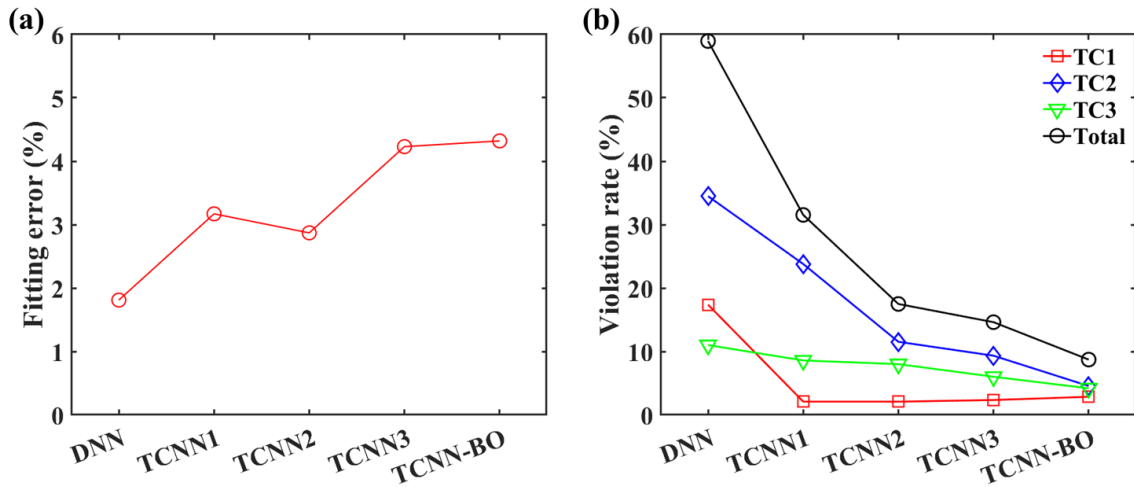


Figure 17. Comparisons of (a) the fitting errors and (b) violation rates across all five implementations of the neural network approaches that were considered here.

## 5. Conclusions

In this paper, we proposed a thermodynamically consistent neural network approach that provides interfacial traction-separation relations in the form of surfaces in traction *vs.* separation amplitude and phase angle space using experimental data that had been obtained along discrete loading paths. The proposed approach not only provides robust surfaces for mixed-mode traction-separation data but also conforms to thermodynamic principles that are directed at the development of damage once the strength of the interface has been exceeded. This is achieved by fusing the neural network model with thermodynamic consistency conditions as constraints. In addition, by integrating Bayesian optimization for the weight factors that reflect the priorities assigned to each constraint, the proposed approach was able to accommodate observed conflicts between the experimental data and thermodynamic consistency. While the fitting errors increased as constraints were systematically applied, they were still less than 5% once Bayesian optimization was applied to the selection of weight factors. In addition, the optimal weight factors also provided the lowest violation rate across all three thermodynamic constraints.

It remains to be seen how effective cohesive zone modeling that embodies the generated surfaces are in predicting the strength and durability of multilayered components that are subject to interfacial failure under mixed-mode fracture conditions.

## Acknowledgements

The authors would like to acknowledge the funding provided by the National Science Foundation under contracts #1930881 (Congjie Wei and Chenglin Wu) and EEC-1160494 (Kenneth M. Liechti). The latter is under the auspices of the National Science Foundation Nanosystems Engineering Research Center on Nanomanufacturing Systems for Mobile Computing and Mobile Energy Technologies (NASCENT). Jiaxin Zhang would like to acknowledge the funding supported by the U.S. Department of Energy, Office of Science, Office of Advanced Scientific Computing Research, Applied Mathematics program; and by the Artificial Intelligence Initiative at the Oak Ridge National Laboratory (ORNL). ORNL is operated by UT-Battelle, LLC., for the U.S. Department of Energy under Contract DEAC05-00OR22725.

## References

- Barenblatt, G. I. (1962). "The mathematical theory of equilibrium cracks in brittle fracture." Advances in Applied Mechanics **7**(1): 55-129.
- Beltz, G. and J. Rice (1991). "Dislocation nucleation versus cleavage decohesion at crack tips." Modeling the Deformation of Crystalline Solids: 457-480.
- Berggreen, C., B. C. Simonsen and K. K. Borum (2007). "Experimental and numerical study of interface crack propagation in foam-cored sandwich beams." Journal of Composite Materials **41**(4): 493-520.
- Brunton, S. L., B. R. Noack and P. Koumoutsakos (2020). "Machine learning for fluid mechanics." Annual Review of Fluid Mechanics **52**: 477-508.
- Camanho, P. P., C. G. Davila and M. De Moura (2003). "Numerical simulation of mixed-mode progressive delamination in composite materials." Journal of Composite Materials **37**(16): 1415-1438.
- Cordisco, F. A., P. D. Zavattieri, L. G. Hector Jr and B. E. Carlson (2016). "Mode I fracture along adhesively bonded sinusoidal interfaces." International Journal of Solids and Structures **83**: 45-64.
- Dong, J., M. Chen, Y. Jin, G. Hong, M. Zaman and Y. Li (2019). "Study on micro-scale properties of cohesive zone in shale." International Journal of Solids and Structures **163**: 178-193.
- Dugdale, D. S. (1960). "Yielding of steel sheets containing slits." Journal of the Mechanics and Physics of Solids **8**(2): 100-104.
- Eggersmann, R., T. Kirchdoerfer, S. Reese, L. Stainier and M. Ortiz (2019). "Model-free data-driven inelasticity." Computer Methods in Applied Mechanics and Engineering **350**: 81-99.
- Elices, M., G. Guinea, J. Gomez and J. Planas (2002). "The cohesive zone model: advantages, limitations and challenges." Engineering Fracture Mechanics **69**(2): 137-163.
- Eriksson, D., M. Pearce, J. Gardner, R. D. Turner and M. Poloczek (2019). Scalable global optimization via local bayesian optimization. Advances in Neural Information Processing Systems.
- Freed, Y. and L. Banks-Sills (2008). "A new cohesive zone model for mixed mode interface fracture in bimetals." Engineering Fracture Mechanics **75**(15): 4583-4593.

Huang, D., J. N. Fuhg, C. Weißenfels and P. Wriggers (2020). "A machine learning based plasticity model using proper orthogonal decomposition." Computer Methods in Applied Mechanics and Engineering **365**: 113008.

Karpatne, A., W. Watkins, J. Read and V. Kumar (2017). "Physics-guided neural networks (pgnn): An application in lake temperature modeling." arXiv preprint arXiv:1710.11431.

Kingma, D. P. and J. Ba (2014). "Adam: A method for stochastic optimization." arXiv preprint arXiv:1412.6980.

Kutz, J. N. (2017). "Deep learning in fluid dynamics." Journal of Fluid Mechanics **814**: 1-4.

Lemaitre, J. (2012). A course on damage mechanics, Springer Science & Business Media.

McGarry, J. P., É. Ó. Máirtín, G. Parry and G. E. Beltz (2014). "Potential-based and non-potential-based cohesive zone formulations under mixed-mode separation and over-closure. Part I: Theoretical analysis." Journal of the Mechanics and Physics of Solids **63**: 336-362.

Mosler, J. and I. Scheider (2011). "A thermodynamically and variationally consistent class of damage-type cohesive models." Journal of the Mechanics and Physics of Solids **59**(8): 1647-1668.

Needleman, A. (1987). "A continuum model for void nucleation by inclusion debonding."

Needleman, A. (1990). "An analysis of tensile decohesion along an interface." Journal of the Mechanics and Physics of Solids **38**(3): 289-324.

Ozaki, Y., Y. Tanigaki, S. Watanabe and M. Onishi (2020). Multiobjective tree-structured parzen estimator for computationally expensive optimization problems. Proceedings of the 2020 Genetic and Evolutionary Computation Conference.

Park, K., H. Choi and G. H. Paulino (2016). "Assessment of cohesive traction-separation relationships in ABAQUS: A comparative study." Mechanics Research Communications **78**: 71-78.

Park, K. and G. H. Paulino (2013). "Cohesive zone models: a critical review of traction-separation relationships across fracture surfaces." Applied Mechanics Reviews **64**(6).

Park, K., G. H. Paulino and J. R. Roesler (2009). "A unified potential-based cohesive model of mixed-mode fracture." Journal of the Mechanics and Physics of Solids **57**(6): 891-908.

Raissi, M., P. Perdikaris and G. E. Karniadakis (2019). "Physics-informed neural networks: A deep learning framework for solving forward and inverse problems involving nonlinear partial differential equations." Journal of Computational Physics **378**: 686-707.

Rose, J. H., J. Ferrante and J. R. Smith (1981). "Universal binding energy curves for metals and bimetallic interfaces." Physical Review Letters **47**(9): 675.

Shahriari, B., K. Swersky, Z. Wang, R. P. Adams and N. De Freitas (2015). "Taking the human out of the loop: A review of Bayesian optimization." Proceedings of the IEEE **104**(1): 148-175.

Snoek, J., H. Larochelle and R. P. Adams (2012). "Practical bayesian optimization of machine learning algorithms." Advances in Neural Information Processing Systems **25**: 2951-2959.

Swadener, J., K. Liechti and Y. Liang (2002). "Shear induced toughening in bonded joints: experiments and analysis." International Journal of Fracture **114**(2): 113-132.

Turon, A., P. Camanho, J. Costa and J. Renart (2010). "Accurate simulation of delamination growth under mixed-mode loading using cohesive elements: definition of interlaminar strengths and elastic stiffness." Composite Structures **92**(8): 1857-1864.

Ungsuwarungsri, T. and W. G. Knauss (1987). "The role of damage-softened material behavior in the fracture of composites and adhesives." International Journal of Fracture **35**(3): 221-241.

Volokh, K. Y. (2004). "Comparison between cohesive zone models." Communications in Numerical Methods in Engineering **20**(11): 845-856.

Wang, Z., D. Xiao, F. Fang, R. Govindan, C. C. Pain and Y. Guo (2018). "Model identification of reduced order fluid dynamics systems using deep learning." International Journal for Numerical Methods in Fluids **86**(4): 255-268.

Weber, G., M. Pinz and S. Ghosh (2020). "Machine Learning-Aided Parametrically Homogenized Crystal Plasticity Model (PHCPM) for Single Crystal Ni-Based Superalloys." JOM: 1-16.

Wittmann, F., K. Rokugo, E. Brühwiler, H. Mihashi and P. Simonin (1988). "Fracture energy and strain softening of concrete as determined by means of compact tension specimens." Materials and Structures **21**(1): 21-32.

Wu, C., R. Huang and K. M. Liechti (2019). "Simultaneous extraction of tensile and shear interactions at interfaces." Journal of the Mechanics and Physics of Solids **125**: 225-254.

Yang, Q. and B. Cox (2005). "Cohesive models for damage evolution in laminated composites." International Journal of Fracture **133**(2): 107-137.

Yang, Y. and P. Perdikaris (2019). "Adversarial uncertainty quantification in physics-informed neural networks." Journal of Computational Physics **394**: 136-152.

Zhao, M. and J. Li (2018). Tuning the hyper-parameters of CMA-ES with tree-structured Parzen estimators. 2018 Tenth International Conference on Advanced Computational Intelligence (ICACI), IEEE.



# Data Driven Modeling of Interfacial Traction Separation Relations using a Thermodynamically Consistent Neural Network Supplementary Information

Congjie Wei<sup>1</sup>, Jiaxin Zhang<sup>2</sup>, Kenneth M. Liechti<sup>3</sup>, Chenglin Wu<sup>1\*</sup>,

<sup>1</sup>Department of Civil, Architectural, and Environmental Engineering  
Missouri University of Science and Technology, Rolla, MO, USA

<sup>2</sup>Computer Science and Mathematics Division

Oak Ridge National Laboratory, Oak Ridge, TN 37830

<sup>3</sup>Center for the Mechanics of Solids, Structures and Materials

Department of Aerospace Engineering and Engineering Mechanics

The University of Texas at Austin, Austin, TX, USA

\* Corresponding author E-mail: [zhangj@ornl.gov](mailto:zhangj@ornl.gov), [wuch@mst.edu](mailto:wuch@mst.edu)

## S1. PPR model fitting with experimental traction separation relations

To explore the possibility of fitting experimental data with existing analytical models, Monte Carlo simulations are used to fit experimentally obtained traction-separation relations with the PPR model. The normal and tangential tractions ( $\sigma_n, \sigma_t$ ) are derived by taking the gradient of the PPR potential and relate to the normal and tangential separations ( $\delta_n, \delta_t$ ) with,

$$\sigma_n = \frac{\Gamma_n}{\Delta_n} \left( m \left( 1 - \frac{\delta_n}{\Delta_n} \right)^\alpha \left( \frac{m}{\alpha} + \frac{\delta_n}{\Delta_n} \right)^{m-1} - \alpha \left( 1 - \frac{\delta_n}{\Delta_n} \right)^{\alpha-1} \left( \frac{m}{\alpha} + \frac{\delta_n}{\Delta_n} \right)^m \right) \left( \Psi_t \left( 1 - \frac{\delta_t}{\Delta_t} \right)^\beta \left( \frac{n}{\beta} + \frac{\delta_t}{\Delta_t} \right)^n + \langle \psi_t - \psi_n \rangle \right) \quad (\text{S1a})$$

$$\sigma_t = \frac{\Gamma_t}{\Delta_t} \left( n \left( 1 - \frac{|\delta_t|}{\Delta_t} \right)^\beta \left( \frac{n}{\beta} + \frac{|\delta_t|}{\Delta_t} \right)^{n-1} - \beta \left( 1 - \frac{|\delta_t|}{\Delta_t} \right)^{\beta-1} \left( \frac{n}{\beta} + \frac{|\delta_t|}{\Delta_t} \right)^n \right) \left( \Psi_n \left( 1 - \frac{\delta_n}{\Delta_n} \right)^\alpha \left( \frac{m}{\alpha} + \frac{\delta_n}{\Delta_n} \right)^m + \langle \psi_n - \psi_t \rangle \right) \frac{\delta_t}{|\delta_t|} \quad (\text{S1b})$$

where,  $\Delta_n, \Delta_t$  are characteristic length scale parameters where the  $\sigma_n, \sigma_t$  decrease to 0,  $\Psi_n, \Psi_t$  are energy constants,  $\psi_n, \psi_t$  are fracture energies where the subscripts  $n$  is for normal and  $t$  is for tangential. The quantities  $\alpha, \beta$  and  $m, n$  are shape parameters and non-dimensional exponents to be determined.

Among these parameters,  $m, n$  are dependent on  $\alpha, \beta$  with:

$$m = \frac{\alpha(\alpha-1)\lambda_n^2}{(1-\alpha\lambda_n^2)}, \quad (\text{S2a})$$

$$n = \frac{\beta(\beta-1)\lambda_t^2}{(1-\beta\lambda_t^2)}, \quad (\text{S2b})$$

where,  $\lambda_n, \lambda_t$  is defined as  $\lambda_n = \Delta_{nc}/\Delta_n, \lambda_t = \Delta_{tc}/\Delta_t$  with  $\Delta_{nc}, \Delta_{tc}$  being the critical opening displacement where the tractions  $\sigma_n, \sigma_t$  reach their peak values. The quantities  $\Psi_n, \Psi_t$  are dependent on  $\psi_n, \psi_t$  as well as  $m, n, \alpha, \beta$ :

$$\Psi_n = (-\psi_n)^{\frac{\langle \psi_n - \psi_t \rangle}{\psi_n - \psi_t}} \left(\frac{\alpha}{m}\right)^m \quad (\text{S3a})$$

$$\Psi_t = (-\psi_t)^{\frac{\langle \psi_t - \psi_n \rangle}{\psi_t - \psi_n}} \left(\frac{\beta}{n}\right)^n \quad (\text{S3b})$$

A total of 8 parameters are totally independent: length scales parameters,  $\Delta_{nc}, \Delta_{tc}$  and  $\Delta_n, \Delta_t$ ; energy parameters,  $\psi_n, \psi_t$ ; non-dimensional parameters,  $\alpha, \beta$ .

While fitting the experimental data with PPR models, we choose these parameters as variables to be optimized based on Eq. S1-S3. For each parameter, a varying range is specified based on the experimental data sets. For each modeling iteration, randomly generated values within each range is assigned to the independent parameters and normal and tangential tractions corresponding to separations along loading paths are calculated and compared to the experimental data. A total of 5.0e6 iterations are calculated and the parameter combination with least error is recorded. It is checked that value of each independent variables are within the range and not too close to either the upper or lower boundaries of the selected range.

As shown in Figure S2, along loading paths, both the normal and tangential tractions have certain errors when compared with the experimental data. The main differences exist at the critical separations where the tractions reach peak values or zero, the Young's modulus and any nonlinearity of the elastic stage and the form of softening stages. These fitting results show that even though this is the most flexible analytical model, the PPR model is still unable to capture the elastic response, the sharp peaks in traction values and the damage characteristics of the extracted traction-separation relations.

## S2. J-Integral conservation

To maintain J-integral conservation, the total J-integral ( $J$ ) is the sum of normal and tangential J-integral components, when the balance condition is satisfied, i. e.,

$$J = \int_{\Gamma} \sqrt{\sigma_n^2 + \sigma_t^2} d\delta = J_n + J_t = \int_{\Gamma} \sigma_n d\delta_n + \int_{\Gamma} \sigma_t d\delta_t, \quad (\text{S4})$$

where  $d\delta = \sqrt{1 + \tan^2 \phi} d\delta_n$ .

According to the phase angle definition Eq. 1b, normal and tangential separations are related through,

$$\delta_t = \tan \phi \delta_n. \quad (\text{S5})$$

Substituting Eq. S5 into Eq. S4 yields

$$\int_r \sigma_n d\delta_n + \int_r \sigma_t \tan \phi d\delta_n = \int_r \sqrt{(\sigma_n^2 + \sigma_t^2)(1 + \tan^2 \phi)} d\delta_n. \quad (\text{S6})$$

Ensuring that Eq. S6 holds for all values of  $d\delta_n$  requires that,

$$\sigma_n + \sigma_t \tan \phi = \sqrt{(\sigma_n^2 + \sigma_t^2)(1 + \tan^2 \phi)}. \quad (\text{S7})$$

Squaring both sides we have,

$$\sigma_n^2 + \sigma_t^2 \tan^2 \phi + 2\sigma_n \sigma_t \tan \phi = (\sigma_n^2 + \sigma_t^2)(1 + \tan^2 \phi), \quad (\text{S8})$$

which leads to,

$$\sigma_n^2 \tan^2 \phi + \sigma_t^2 - 2\sigma_n \sigma_t \tan \phi = 0. \quad (\text{S9})$$

Thus,

$$(\sigma_n \tan \phi - \sigma_t)^2 = 0, \quad (\text{S10})$$

thereby yielding:

$$\frac{\sigma_t}{\sigma_n} = \tan \phi = \frac{\delta_t}{\delta_n} \quad (\text{S11})$$

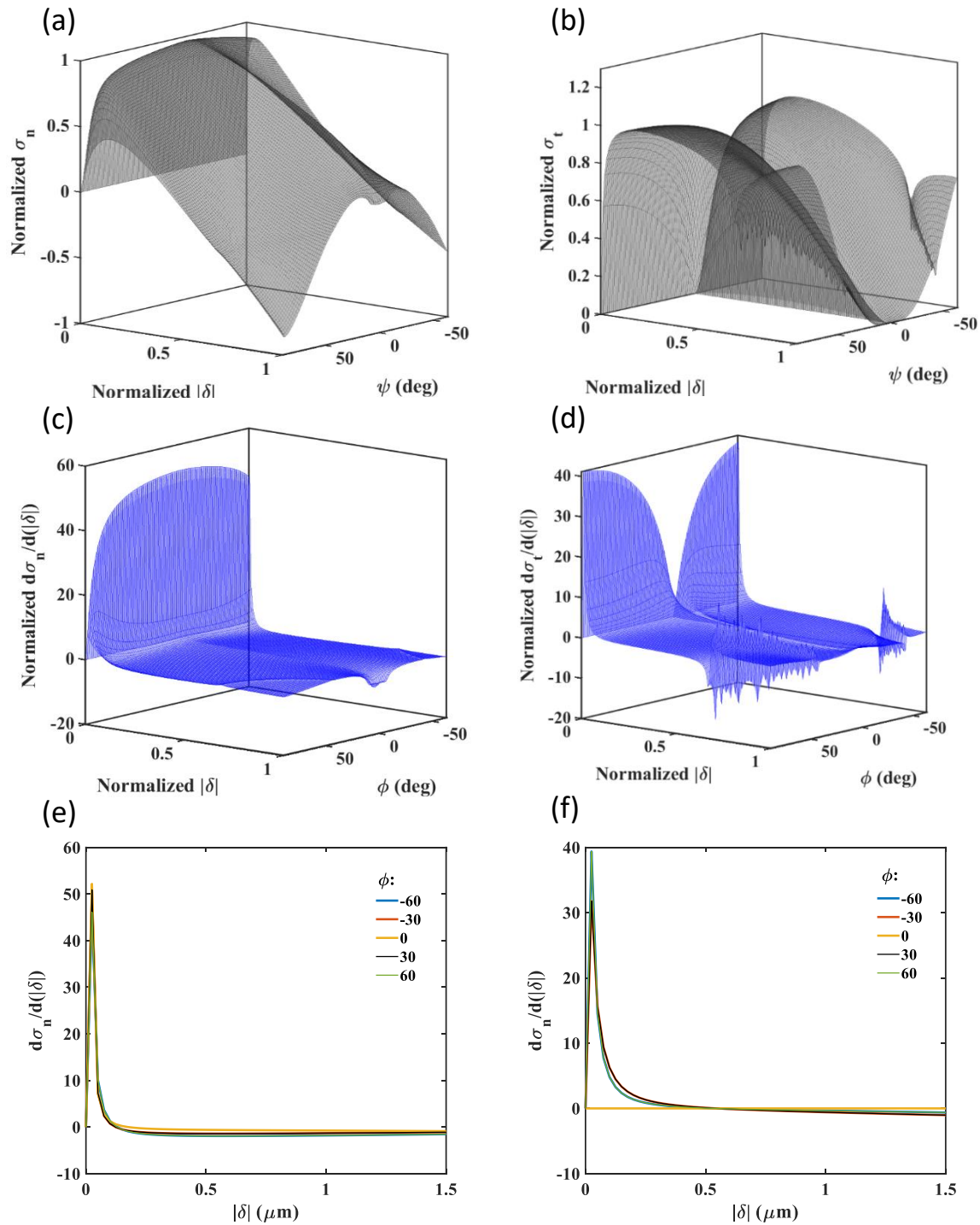


Figure S1. Normalized PPR model for (a) normal and (b) shear traction as a function of phase angle ( $\phi$ ) and absolute separation ( $|\delta|$ ). Gradient surfaces for (c) normal and (d) shear tractions. (e-f) Gradient of (e) normal and (f) shear tractions for loading paths along certain phase angles.

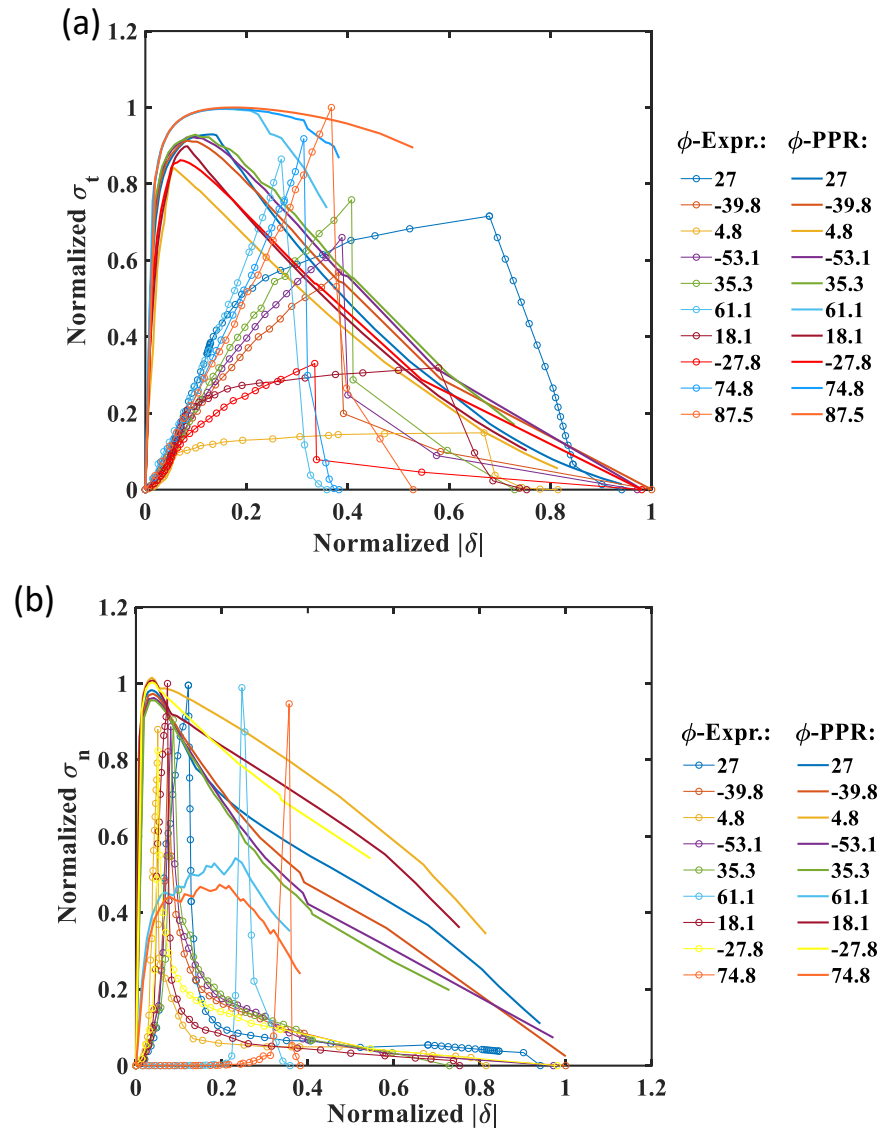


Figure S2. Comparison of extracted and PPR representations of (a) normal and (b) shear tractions along the loading paths that were taken in the experiments.